Modelling firebrand dynamics in a coupled Fire-Atmosphere models: an Eulerian approach

Alberto Alonso-Pinar[1,5], Jean-Baptiste Filippi[1], Adrien Guyot[2], Nicholas McCarthy[3], Pierre Tulet[4], and Alexander Filkov[5]

[1]SPE UMR6134, Université de Corse, Campus Grimaldi, Corse, France
[2]Australian Bureau of Meteorology, Melbourne, Victoria, Australia
[3]Country Fire Authority, Burwood East, Victoria, Australia
[4]CNRM Météo France, Toulouse, France
[5]Faculty of Science, The University of Melbourne, 4 Water St., Creswick, Victoria, Australia

Correspondence: Jean-Baptiste Filippi (filippi_j@univ-corse.fr)

Received: 1 October 2025 – Discussion started: 17 December 2025
Revised: 27 April 2026 – Accepted: 9 November 2026 – Published:

Proof only

Abstract. Spotting, the process by which burning firebrands are lifted by convection and transported downwind igniting secondary fires, can become a critical driver of rapid wildfire spread and presents major challenges for prediction and suppression. Coupled Fire-Atmosphere models, which simulate the two-way interaction between fire behaviour and local atmospheric dynamics, offer a promising avenue to capture such complex processes. In this study, we introduce a computationally efficient Eulerian formulation for firebrand transport, implemented within the coupled MesoNH–ForeFire modelling framework. Two case studies were analysed: an idealized scenario over flat and hilly terrain to assess orography influence, and a realistic simulation of the 2016 Mt Bolton wildfire in southeastern Australia. The model captured key spotting dynamics and fire spread patterns, producing realistic downwind distances with spot fire timing that slightly preceded observations. A full 8 h forecast, including spotting, simulates in just less than 3 h, without optimization. Results demonstrate that this simplified approach provides a credible and time-efficient firebrand deposition forecast.

1 Introduction

During a wildfire, bark fragments, needles, and branches can ignite and detach from trees, creating firebrands or embers. These firebrands can be lifted by the plume and transported, travelling beyond the main fire, and igniting new fires. This process, known as spotting, complicates fire control, especially with medium and long-range spotting (Koo et al., 2010). Following the definition from Cruz et al. (2015), medium range spotting refers to spot fires located at distances between 750 and 5000 m, and long-range spotting refers to spot fires located at distances greater than 5000 m. In both cases, it refers to spot fires that are not overrun by the main fire front. The challenge of predicting the final distance and direction over which firebrands might land and ignite the fuel bed has been the focus of many experimental and numerical studies (Albini, 1979; Albini et al., 2012; Kepert et al., 2024).

Firebrand transport has been investigated through three principal modelling frameworks: Lagrangian firebrand modelling, mathematical analogue models (similar to the classification offered by Sullivan, 2009), and Eulerian approaches. Lagrangian models calculate the trajectories of individual firebrands to estimate parameters regarding the maximum travelled distance, lateral displacement, and ground landing densities. Early models from (Albini, 1979, 1983, 1981; Noble et al., 1980) offer an estimation of the maximum spotting distance under specified fuel and weather conditions. More complex simulations, however, require accurate wind flow characterization, often prescribed using semi-empirical relationships such as the logarithmic wind profile (Himoto and Tanaka, 2005; Sardoy et al., 2007, 2008; Bhutia et al., 2010; Oliveira et al., 2014). More advanced Computational Fluid Dynamics (CFD) and Large Eddy Simulations (LES) have also been used to calculate realistic wildfire

plumes in order to compute firebrand trajectories (Thurston et al., 2017; Thomas et al., 2020; Cervantes, 2023; Alonso-Pinar et al., 2025a). These models have provided insights on the spotting distance, the impact of turbulence, and the implications of physical and numerical models to describe the firebrand trajectories. However, they are numerically expensive due to the requirement of a relatively small timestep, and a large number of firebrands to obtain statistically robust outcomes. To address this, Frediani et al. (2025) proposed a parametrization approach to model individual firebrands advected by the wind flow. Their results show that accounting for spotting increased the overall accuracy of wildfire behaviour simulations.

Spotting parametrizations have also been developed using mathematical analogue models, such as cellular automata models (López-De-Castro et al., 2024). The parametrizations are often informed by firebrand distributions fitted on Lagrangian simulations (Sardoy et al., 2008). For example, the spotting model proposed by Trucchia et al. (2019) also made use of a log-normal distribution to generate spot fires. In doing so, they developed a stochastic formulation intended for operational wildfire simulators. More recently, Kepert et al. (2024) have provided a novel parametrization of a firebrand transport model based on simulations of Lagrangian particles within high-resolution LES simulations of wildfire plumes. These models are computationally efficient, but they do not represent all physical phenomena (pyroconvection, plume development) due to the differences in terms of spatial and temporal scales.

High-fidelity modelling approaches that resolve all 6 degrees of freedom of the firebrand may be appropriate for small-scale simulations like (Anand et al., 2018) or analyses of individual firebrand trajectories linked to specific spot fires (Lareau, 2025). However, such complexity and computational cost is generally impractical for coupled Fire–Atmosphere models intended for real-time or faster-than-real time wildfire forecasting (Alonso-Pinar et al., 2025a; Oliveira et al., 2014). To overcome this limitation, the Eulerian approach that transports a firebrand concentration field on a grid by using a diffusion-advection equation can be used. To the knowledge of the authors, this approach has been used in a wildfire context only by Qin and Trouvé (2025) to transport firebrands in a bidimensional landscape using a stochastic approach to derive the ember flight distance. The Eulerian approach has the advantage of being simpler to implement numerically and faster to calculate, as it can be computed simultaneously with the coupled Fire-Atmosphere simulation. This method also allows the inclusion of physical processes, such as the firebrand combustion and associated reduction in firebrand mass, or the mixing of firebrands from different sources. Similar methodologies have been successfully employed in the transport of relatively heavy particles, such as pollen (Dupont et al., 2006) or volcanic ashes (Costa et al., 2006).

Coupled Fire-Atmosphere models have been designed to enhance the understanding of large-scale wildfire behaviour and to inform operational fire-management strategies (Filippi et al., 2018; Kochanski et al., 2021, 2016, 2011). These models have demonstrated applicability across a broad spectrum of spatial scales, spanning from grassland fires (Filippi et al., 2013; Kochanski et al., 2011) to very large wildfires (Filippi et al., 2018; Kochanski et al., 2013; Peace et al., 2023, 2022, 2016). Moreover, they have effectively captured specific terrain influences on fire spread (Simpson et al., 2014, 2013), complex dynamic fire behaviours (Thomas et al., 2017), and the formation of highly convective plumes (Couto et al., 2024). Despite these advances, current implementations do not yet incorporate parametrizations for firebrand transport or the broader spotting phenomenon.

In the present study, we aim to introduce a simple Eulerian model that describes the firebrand transport. The main goal is to introduce and evaluate the model using both idealized and realistic case studies. To achieve this goal, several objectives are identified: perform a comparison between the Lagrangian and Eulerian approaches in terms of deposited firebrands and computational costs, perform a comparison between the Radar observations and the simulation results, and finally to perform a comparison of spot fires between the Eulerian approach and field observations. The Eulerian model is first evaluated using idealized wildfire simulations. It is then validated against the Mt Bolton wildfire in southeastern Australia, described in detail by McCarthy et al. (2018). The fire was chosen for its unique extensive observational dataset, which allowed for thorough model verification and evaluation. The paper is organized as follows. Section 2 introduces the modelling framework and the simulation setup. Section 3 presents the results obtained for both the idealized and real simulations. Finally, the results from the idealised simulations and the Mt Bolton fire are discussed in Sect. 4.

2 Methods

2.1 Coupled Fire-Atmosphere framework

The atmospheric simulations in this study were performed using the coupled Fire-Atmosphere model MesoNH-ForeFire (Filippi et al., 2011; Lac et al., 2018), version 5-7-2. Meso-NH is an anelastic and non-hydrostatic meso-scale model (Lafore et al., 1998) that can be used in a large set of spatial scales, resolving weather phenomena ranging from characteristic lengths of 10 to 10 000 m. Meso-NH is used in a Large Eddy Simulation (LES) configuration, resolving the large structures from the wind flow perturbed by the surface fire. Wind velocities are transported by a 4th order centered scheme, and the other variables (potential temperature, TKE, mixing ratios) by the PPM scheme (Piecewise Parabolic Method from Colella and Woodward, 1984). Temporal derivatives are computed following a 4th order Runge–

Proof only

Kutta centered scheme. Finally, the turbulence parameterization is based on a 1.5-order closure with a prognostic equation for the 3D Turbulent Kinetic Energy (Lac et al., 2018).

ForeFire is a fire spread model that calculates the temporal evolution of a fire front using Lagrangian markers. The model takes into account terrain slope, fuel spatial arrangement and fuel combustion parameters, and surface winds coming from Meso-NH (Filippi et al., 2009). At each atmospheric timestep, ForeFire outputs heat and vapor fluxes to the atmospheric model. The rate of spread is calculated using the Rothermel model (Rothermel, 1972).

2.2 Firebrand modelling

The following paragraphs describe how spotting is modelled within MesoNH-Forefire.

2.2.1 Firebrand injection

Firebrand generation is a complex phenomenon that has been modelled only for twigs and branches (Barr and Ezekoye, 2013). Empirical data on firebrand generation remains sparse, with limited experimental or field observations available (Filkov et al., 2017). In the present study, firebrand injection into the atmosphere is prescribed as a firebrand mass flux (in $\mathrm{kg\,m^{-2}\,s^{-1}}$), originating from the bottom ground level of the atmospheric model. Injection is assumed to occur over a fixed duration of 60 s, during which firebrand mass flux is held constant at $1\,\mathrm{kg\,m^{-2}\,s^{-1}}$. TSI ally, a time lag is introduced between the fire front reaching a given grid cell and the initiation of the firebrand injection. The delay time is set to 30 s, based on Fig. 7 from Filkov et al. (2017), where firebrand detection follows an increase in the mean wind value, representative of the fire front arrival.

The numerical implementation relies on ForeFire (Filippi et al., 2013) and is designed to remain flexible for future extensions. For instance, variables such as fire intensity or local turbulent kinetic energy could be incorporated to control the firebrand mass flux, along with fuel type, injection duration, and time delay. These relationships could be derived from laboratory studies (Ju et al., 2023), field observations (Filkov et al., 2017), or inverse analysis using CFD simulations (Wickramasinghe et al., 2022).

2.2.2 Firebrand transport

In the Eulerian model, firebrands are considered as a continuous concentration field. Its spatiotemporal evolution is described by an advection conservation Eq. (1). Where ρ_{ref} is the reference air density, C_i is the concentration of the ith firebrand class, U is the advecting wind vector ($\mathrm{m.s^{-1}}$) given by $(u, v, w - w_{\mathrm{g}})$ where u is the zonal velocity, v the meridional velocity, w the vertical velocity and w_{g} the firebrand terminal velocity. S_i is the source and sink terms (corresponding to the injection and deposition of firebrands). The equation is written for a general number of firebrands (index i), as the modelling options could include multiple types of firebrand densities, or different firebrand states (burning and non-burning firebrands, for instance).

$$\frac{\partial\left(\rho_{\mathrm{ref}} C_i\right)}{\partial t} + \nabla\left(\rho_{\mathrm{ref}} C_i U\right) = \rho_{\mathrm{ref}} S_i \tag{1}$$

The advection of the firebrand concentration field is calculated using the piecewise parabolic method (PPM). Specifically, the PPM scheme used here incorporates the flux limiter (Skamarock, 2006). When using this scheme in Meso-NH, numerical diffusion of the scalar field is not activated to prevent damping of well resolved extrema (Lac et al., 2018).

Firebrand concentration and air parcel relative velocity is represented by the addition of a vertical terminal velocity to the wind flow (Tarifa et al., 1967, 1965; Thomas et al., 2020). In this study, the Eulerian model accounts for a single firebrand species with a mean vertical terminal velocity given by Eq. (2). Using $g = 9.81\,\mathrm{m\,s^{-2}}$, $\rho_0 = 350\,\mathrm{kg\,m^{-3}}$, $\rho_{\mathrm{atm}} = 1.2\,\mathrm{kg\,m^{-3}}$, and an adjustment factor lambda 0.0023 (Alonso-Pinar et al., 2025b), the resulting terminal velocity was $3.2\,\mathrm{m\,s^{-1}}$. Rotational impacts and aerodynamic lift are neglected.

$$w_{\mathrm{g}} = \sqrt{2g\frac{\rho_0}{\rho_{\mathrm{atm}}}\lambda} \tag{2}$$

2.2.3 Firebrand deposition

Deposition is obtained through a temporal integration of this firebrand mass flux at the ground cell. Specifically, the sum of all values is computed, which corresponds to the total instantaneous flux of particles reaching the ground over the domain. This quantity is multiplied by the atmospheric time step, providing the amount deposited during that time increment. The result is accumulated over time to produce a cumulative deposition: a simulation output variable is obtained every 20 s to limit disk writing.

Two separate accumulations are performed: one for injected particles from the ground and one for deposited particles. In both cases, the method is equivalent: deposition is calculated as the time integral of the spatially integrated ground flux, assuming that the flux is uniformly distributed over each grid cell and constant within an atmospheric time step.

2.3 Simulations setup

An idealized simulation was first conducted using Meso-NH – ForeFire. The objective was to investigate the results of the Eulerian model on two different idealized topographies: a flat and a hill terrain. Fire progression is fixed, and the feedback from the atmosphere into the fire is not accounted for. The fuel bed was assumed homogeneous with a nominal heat flux of $80\,\mathrm{kW\,m^{-2}}$. Open boundary conditions were selected for all configurations. Atmospheric conditions were spun-up using a simulated atmospheric profile,

Proof Only

specifying wind speeds and dry potential temperatures at two distinct heights: 100 and 150 m. The inflow wind is assumed to be purely longitudinal with the transverse (v) component equal to 0, with the 100 m wind (10 m-s^{-1} in this study) serving as the reference. The computational domain is 28.8 km × 14.4 km × 15.8 km with a horizontal resolution of 80 m (Baggio et al., 2022). More details regarding the model configuration and numerical settings can be found in Alonso-Pinar et al. (2025b, a).

A preliminary set of simulations were performed using the idealized configuration to study the mass conservation of the Eulerian model. By accumulating the injection and deposition of firebrands during the simulation, it was possible to calculate their difference and evaluate the firebrand mass loss. It was found that the numerical scheme influenced the mass loss. Among the three available numerical schemes (Lac et al., 2018), the unrestricted PPM00, the monotonic version PPM01 and a monotonic scheme with a flux limiter PPM02, the latter conserved 96 % of the injected firebrand mass. At the scale of the full simulation, this residual was considered sufficiently small that it does not affect the main conclusions of the study

A second simulation was conducted to reproduce the Mt Bolton fire (McCarthy et al., 2018). The vertical grid consists of 50 levels, gradually stretching from 30 m at the bottom, to 900 m at the topmost grid cell, following previous studies from Couto et al. (2024) and Baggio et al. (2022). The simulation was performed with three nested grids using a two-way coupling. Boundary conditions of the large domain were initialized with ERA5 dataset every hour (Hersbach et al., 2023). The simulation spin-up was done from 08:00 to 13:00 AEDT local time (LT)[1], leaving enough time to initialize the smallest domain. The large domain is of size 120 × 120 cells and a horizontal resolution of 2000 m. The second domain is of size 150 × 150 cells and resolution of 400 m, and the third domain containing the wildfire is of size 150 × 150 cells and resolution of 80 m. Model outputs were saved every 20 s for the small domain, every 120 s for the medium domain and 300 s for the large domain. The smallest domain is centered on the point of coordinates (−37.413, 143.746) and contains the whole fire burnt perimeter on its northwest quadrant, providing enough space to capture the details of the fire generated plume. The wildfire was coupled exclusively to the innermost domain, however, scalar fields representing fire-induced fields (firebrand mass concentration or plume smoke) were advected across all domains. In the large domain, the numerical timestep is set to 10 s, and the one-dimensional sub-grid turbulence parametrization follows the length-scale formulation of Bougeault and Lacarrere (1989). For the two smaller domains, the three-dimensional sub-grid turbulence parametrization is given by the Deardorff mixing length (Cuxart et al., 2000).

Fuel description is derived from the ESA World Cover at a 10 m spatial resolution. Four main land cover classes were identified: grassland, forest, artificial surfaces and constructions, and water bodies. Although a refined fuel description is necessary for detailed fire-progression simulations, this was considered beyond the scope of a study aimed primarily at demonstrating the Eulerian formulation. In Meso-NH – ForeFire, the fire model continues to burn as long as there is available fuel in its propagation direction. Suppression actions during the Mt Bolton fire, which aimed to limit fire progression, were not included in the simulations presented here. Consequently, the available combustible fuel was limited to the burn area of the observed fire: all fuels outside this perimeter were classified as "artificial surfaces" to stop the fire progression such that the spotting transport process could be evaluated in isolation.

Flame residence time was fixed to 250 s with a nominal heat flux of 60 kW m^{-2}. The nominal vapor flux was set to 0.005 kg m^{-2} s^{-1}, resulting in a total mass to be vaporized of 1.25 kg m^{-2}. The firebrand injection flux was set to 1.0 kg m^{-2} s^{-1} for the forest fuel class and to 0.0 kg m^{-2} s^{-1} for the grassland fuel class (Filippi et al., 2013). The fire was initialized as a point ignition at coordinates (−37.37148, 143.70531) and on 23 February 2016 13:15 (23 February 2016 02:15 UTC). Fire propagation was governed by local winds and topography, but the fuel map was constrained to the extent of the final burn perimeter. A separate simulation was performed without fire propagation, to analyse the impact of fire on the atmospheric circulations.

The Mt Bolton namefiles are published accompanying the MesoNH-ForeFire repository as an open-source dataset. The simulation setup is summarized in Table 1.

2.4 Mt Bolton fire overview and observational data

A short overview of the fire behaviour and dynamics is given below. A more complete and detailed description can be found in the study of McCarthy et al. (2018). The Mt Bolton fire was first reported at 13:45 and burnt 126 ha during the first 30 min. The fire initially propagated fast through heterogeneous patches of mixed stubble, grass, and eucalypt woodland areas within the 14:15 perimeter (see Fig. 3). Later, winds shifted from north-westerly to westerly, changing the fire direction and redirecting it through a more continuous eucalypt woodland fuel (with dominant *Eucalyptus obliqua* and sub-dominated *Eucalyptus rubida*) mixed with small pine forest blocks within the 14:33 perimeter (see Fig. 3). During this phase, the fuel supported intense short range (less than 1 km) spotting and increased the burnt area rate of spread to 7 ha min^{-1}. Between 14:33 and 15:30, the burnt area rate of spread reduced to 4 ha min^{-1}. Burnt area spread accelerated again between 15:30 and 16:30, reaching 5 ha min^{-1}, with reported spotting activity likely originating

[1]Local Time (LT) is used throughout the article. LT refers to Australian Eastern Daylight Time (UTC+11), which accounts for daylight saving.

Proof only

Table 1. Parameters used to configure Meso-NH.

Simulation parameter	Value
Large domain – Number of grid points	$120 \times 120 \times 50$ DX = DY = 2000 m
Medium domain – Numbe rof grid points	$150 \times 150 \times 50$ DX = DY = 400 m
Small domain – Number of grid points	$150 \times 150 \times 50$ DX = DY = 80 m
Time step	10 s for large domain 2.5 s for medium domain 0.625 s for small domain
Boundary conditions	Open for all 4 lateral surfaces. Initialization using ERA-5 reanalysis.
Turbulence configuration	1D for the large domain. Turbulence parametrization comes from Bougeault and Lacarrere (1989). 3D where the turbulent mixing length is equal to the cubic root of the grid volume. Turbulence parametrization comes from Cuxart et al. (2000).

from the top of the hill. Post field surveys identified eight distinct long distance spot fires that occurred outside of the final burn perimeter, with the most distant spot fires located 6 km from the fire front.

The fire perimeter was estimated by the Country Fire Authority (CFA) ground observer teams at 14:15 and 15:30. Aerial observations recorded the fire perimeter at 14:33, followed by multispectral line scans at 16:30 and 18:30. The resulting fire progression is shown in Fig. 3.

Detailed measurements of the fire plume were done with a mobile dual-polarized Doppler X-band radar, referred to as UQ-XPOL (Soderholm et al., 2016). UQ-XPOL was deployed to the Mt Bolton fire at 13:45, approximately 5 km to the west of the fire location (see Fig. 3a for the scan bearing line). UQ-XPOL was set to conduct scans in Range Height Indicator (RHI) mode, capturing vertical cross sections of the plume along a given azimuth. Data starting at 15:15 until 16:15 were used here as the radar azimuth was perfectly aligned along the wildfire plume azimuthal axis. Within the scope of this study, radar echoes are used to assess the simulated convective plume, and the segmentation of polarimetric radar data (Guyot et al., 2023) is used to assess the plume contents, distinguishing hydro- and pyro-meteors as presented in McCarthy et al. (2020). Wind flow velocities were also derived by comparing two successive frames of the measured reflectivity over the scan duration.

Although the final burnt perimeter of the Mt Bolton fire was relatively small, the event exhibited several characteristics of *extreme fire behaviour* (Peace et al., 2022; Werth et al., 2016, 2011), making it a valuable case for verification studies. During certain periods, the wildfire demonstrated intense crown fire activity, which produced convective plumes and generated multiple spot fires.

2.5 Evaluation and validation of the model

The Eulerian transport model was evaluated on a set of idealized experiments with a fire forcing the atmosphere in two different idealized topographies: a flat terrain and a hill terrain. The Eulerian model is compared against a Lagrangian model that contains a description of the firebrand aerodynamic and combustion behaviour (Alonso-Pinar et al., 2025a). To describe the aerodynamics effect, the drag model from Haider and Levenspiel (1989) is chosen. The combustion model from Oliveira et al. (2014) was chosen to calculate the size reduction of the firebrand. The firebrand characteristics (length, height, density) are randomly assigned based on existing literature and a previous numerical study on Lagrangian simulated firebrands (Alonso-Pinar et al., 2025a). To perform the comparison, longitudinal and lateral travelled distances are compared between the two models and the Fraction Skill Score, a measure of the spatial and intensity accuracy of a model, is used to conclude (Roberts and Lean, 2008). FSS provides a measure of the forecast skill (in this case the Eulerian approach) against spatial scales for a given threshold intensity. The score has a range between 0 (zero skill forecast) and 1 (perfect skill forecast). In both cases, firebrands were injected from the same area (Lagrangian firebrands' initial position was randomized following Alonso-Pinar et al., 2025a) and during the same time interval (firebrands were injected from 18 000 s until 18 600 s since the beginning of the simulation).

The model is then verified based on the simulations of Mt Bolton wildfire. Firebrands were injected using the parametrization explained in Sect. 2.2.2 and 2.3. A first evaluation of the model is done by comparing radar echoes to the simulation results. The firebrand fields are compared in terms of maximum reached height and lateral displacement. A qualitative comparison is then performed between the reported spot fires produced during the wildfire event and the ground landing densities of firebrand mass flux obtained as a cumulative function of time. A choice was made to accumulate values every 30 min. This choice results from balancing the atmospheric and firebrand time dynamics and a time interval that can be useful in an operational context.

Finally, to assess the realism of the simulation, model results are evaluated against visual observations and radar measurements. Specifically, the atmospheric model computes the liquid mixing ratio within a given atmospheric grid cell defined as the sum of the rain drops ratio and cloud droplets ratio as parametrized by the ICE3 microphysics scheme (Caniaux et al., 1994; Pinty et al., 2001). This provides an indication of liquid water content and can be directly compared to radar measurements. In addition, simulated TKE contours

Proof only

are used to identify and locate the regions of high turbulence within the plume. We compared the simulated plume to observations by using the plume top height, defined in the simulation as the maximum cell height containing at least $0.01\,g\,kg^{-1}$ of smoke (a passive tracer injected at the fire location). To assess pyroconvective episodes of the plume, we analyse the temporal evolution of the fraction of the grid cell surface area containing at least 0.005 g of deposited firebrand mass relative to the total injection surface area. Finally, fire progression contours are compared to conclude on the realism of the simulation.

3 Results

3.1 Idealized cases

The firebrand accumulated and normalized mass ground landing distribution for the Eulerian and Lagrangian models is presented in Fig. 1. The mass ground landing distribution was normalized by the total mass injected. Figure 1a shows the results for the flat terrain and Fig. 1b shows the results for the hilly terrain. For the Eulerian model, values lower than 10^{-4} kg were set to 0 to simplify the figures and the corresponding analysis.

Results for the flat terrain show that the distribution shapes are similar, with most of the firebrands landing near the injection point. From 5.0 to 7.5 km, the distribution of firebrands follows a narrow column of constant width. After this, firebrands land within a cone that expands laterally in the streamwise direction. Maximum longitudinal travelled distance is 14.8 and 15.0 km, and the maximum lateral spread is 1.8 and 2.0 km, respectively, for the Lagrangian and Eulerian models.

Regarding the hilly terrain, the ground mass distribution shapes show some differences between 10.0 and 15.0 km with a wider spread for the Eulerian results. However, the longitudinal and lateral spread are similar between 15.0 and 22.5 km and the general shape of the ground mass distribution are comparable for both models. Maximum longitudinal travelled distance is 18.6 and 18.4 km, and the maximum lateral spread is 1.7 and 1.9 km, respectively, for the Lagrangian and Eulerian model.

For both terrains, the shape corresponds to a bimodal distribution with a first peak located near the injection point (located at approximately 4.8 km longitudinally) and a second peak located at approximately 7.5 and 10 km longitudinally for the Lagrangian and Eulerian models, respectively. Although the shape obtained with the hilly terrain is also bimodal, its tail reaches greater distances longitudinally.

Regarding the computational cost, the Lagrangian approach requires to calculate the atmospheric wind flow (approximately 60 min, with 280 processors) and then calculate the firebrand trajectories (approximately 10 h), while the Eulerian approach calculates both at the same time in an approximate computational time of 70 min with 280 processors.

The Fraction Skill Score (FSS) is presented in Fig. 2. In this study, in both cases, FSS is higher for higher threshold values and decreases for lower values. Across all thresholds and spatial scales greater than 1, FSS values are above 0.7. At the highest threshold of 1, the FSS values are higher for the flat terrain compared to the hill terrain values. For the other intensity thresholds, the FSS values are higher for the hill terrain compared to the flat terrain values. Overall, FSS values at scales of 3 or 5 cells, can be considered as satisfactory, implying that the Eulerian formulation matches the Lagrangian results at scales of 240 to 400 m.

3.2 Mt Bolton wildfire

3.2.1 Fire progression

A comparison between the observed fire progression and the simulated fire perimeters from the coupled simulation is presented in Fig. 3. During the early stages of the event, corresponding to the 14:15 and 14:33 perimeters, the simulated fire progression is slower than the observed fire progression and the burnt perimeter is smaller. Indeed, the observed fire has already reached the limit of its mapped longitudinal spread (north-south axis) and has begun progressing towards the east. This is not captured in the simulation, where the fire is still progressing towards the south. In the simulation, the wind shift starts at approximately 15:02 and ends at 15:26. At the 15:30 perimeter, the observed fire progressed towards the east, and the simulation also showed this behaviour. However, a discrepancy remains in terms of fire spread rate. The 15:30 simulated fire perimeter is behind the actual 15:30 fire perimeter by an estimated distance of 0.5 km. At the 16:30 linescan, the observed fire progression is close to its final burnt area. The simulation results still present a time delay, with fire perimeters behind the actual fire progression.

3.2.2 Plume behaviour

The simulation reveals three distinct periods of intense pyroconvective activity associated with plume development: from 14:13 to 14:31; from 14:53 to 15:48; and from 16:06 to 16:25. These phases are characterized by the development of a large convective plume above the fire perimeter. During the first convective period, the plume centreline ascends to approximately 1.5 km above ground level (a.g.l.) with the maximum plume height reaching 2.5 kma.g.l.. The second episode of intensive convective plume activity starts shortly before the wind shift (starting at 15:02 in the simulation). During this period, the plume centreline ranges from approximately 1.5 kma.g.l. at the beginning to 3.0 km at the end, with the plume height reaching 5.0 kma.g.l. at its highest activity. Finally, the third period corresponds to a situation where the wind has already shifted to the west. In this case, the plume

Proof only

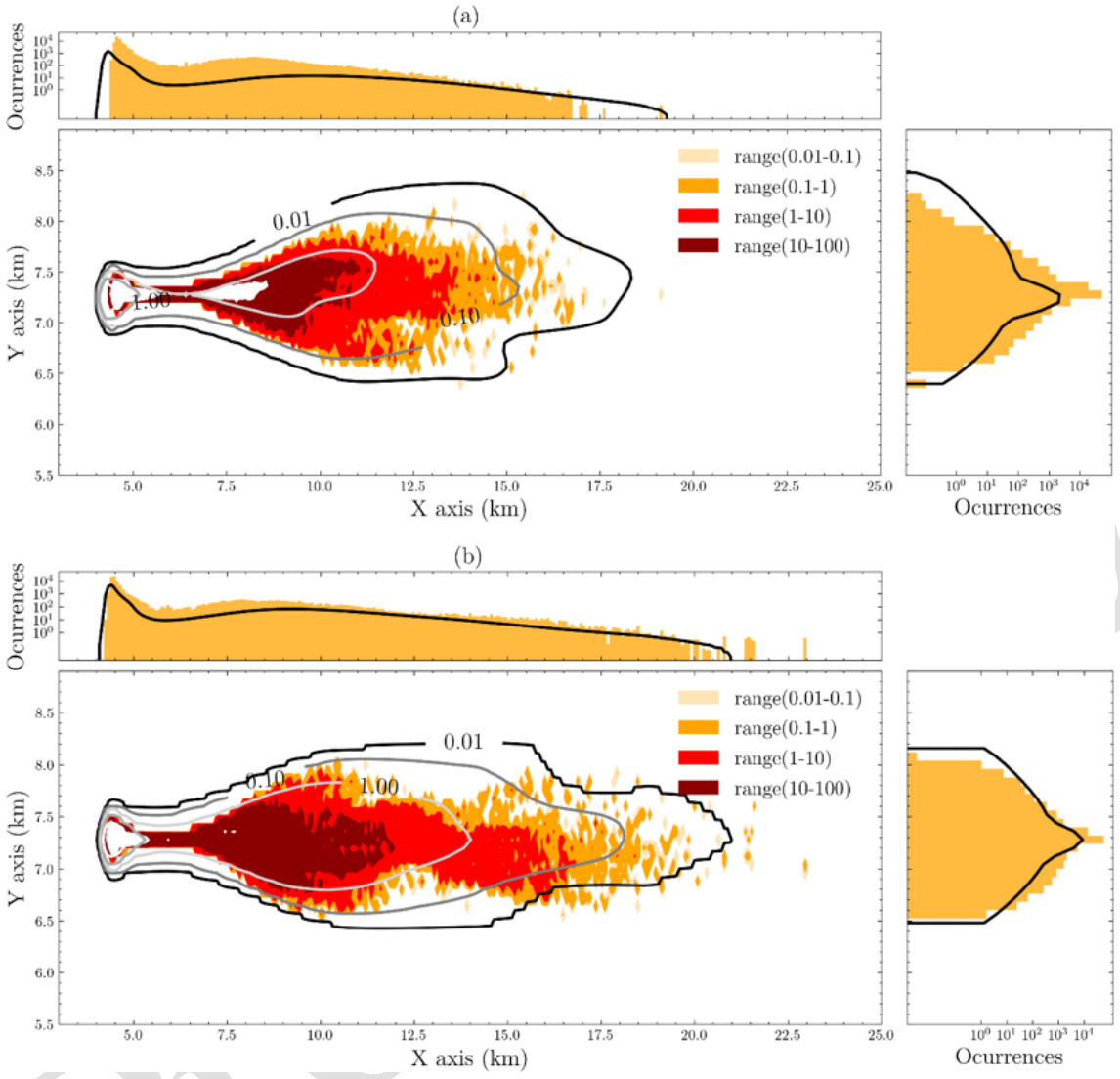


Figure 1. Landing normalized mass densities of the Lagrangian (orange contours) and Eulerian (blackgrey lines) model for ranges between 0.01 and 0.1 kg, 0.1 and 1.0 kg, 1.0 and 10.0 kg, and 10.0 and 100.0 kg, and histogram of longitudinal (top) and axial (right) landing densities, for the flat terrain **(a)** and for the hill terrain **(b)**.

centreline goes up to 2.0 km a.g.l., and the plume maximum height reaches 3.0 km a.g.l. Figure 4 shows a photo of the fire plume at 15:40. Large entrainment wind values are seen in the simulation, reaching values up to 15 m s^{-1}.

The UQ XPOL portable weather radar was deployed and able to capture cross sections of the plume centreline (RHI) during this period (McCarthy et al., 2018). McCarthy et al. (2020) conducted a classification of the polarimetric radar echoes within the fire plume using a Gaussian Mixture Model (GMM) approach that enabled the separation of hydro- and pyro-meteors (McCarthy et al., 2020). The results of the segmentation are presented in Figs. 5a (at 15:15) and 6a (at 15:42), where GMM classes of values 7 and 8 represent the pyrometeors in an ascending or falling mode. Figures 5b and 6b present a side view of the simulation with the same angle as the radar scan bearing line but located 1 km to the south. Figures do not correspond to the same timestamps as the radar observations, but both are extracted at the same time delay of 29 minutes after the radar observations. The spatial and temporal translation was done to overcome the differences of fire progression between the observed and the simulated fire as presented in Fig. 3.

In both Figs. 5a and 6a, suspended water is present. Based on the GMM classification, pyrometeors are lifted at heights between 1 and 3 km a.g.l. occupying the central region of the plume. Longitudinally, pyrometeors are transported up to 5 km (from 5.0 to 10.0 km), corresponding to the reported spot fire distances during the fire. Water content at high altitudes shows that the plume developed into a pyrocumulus cloud (pyroCu). In Fig. 5a, water content is detected at dis-

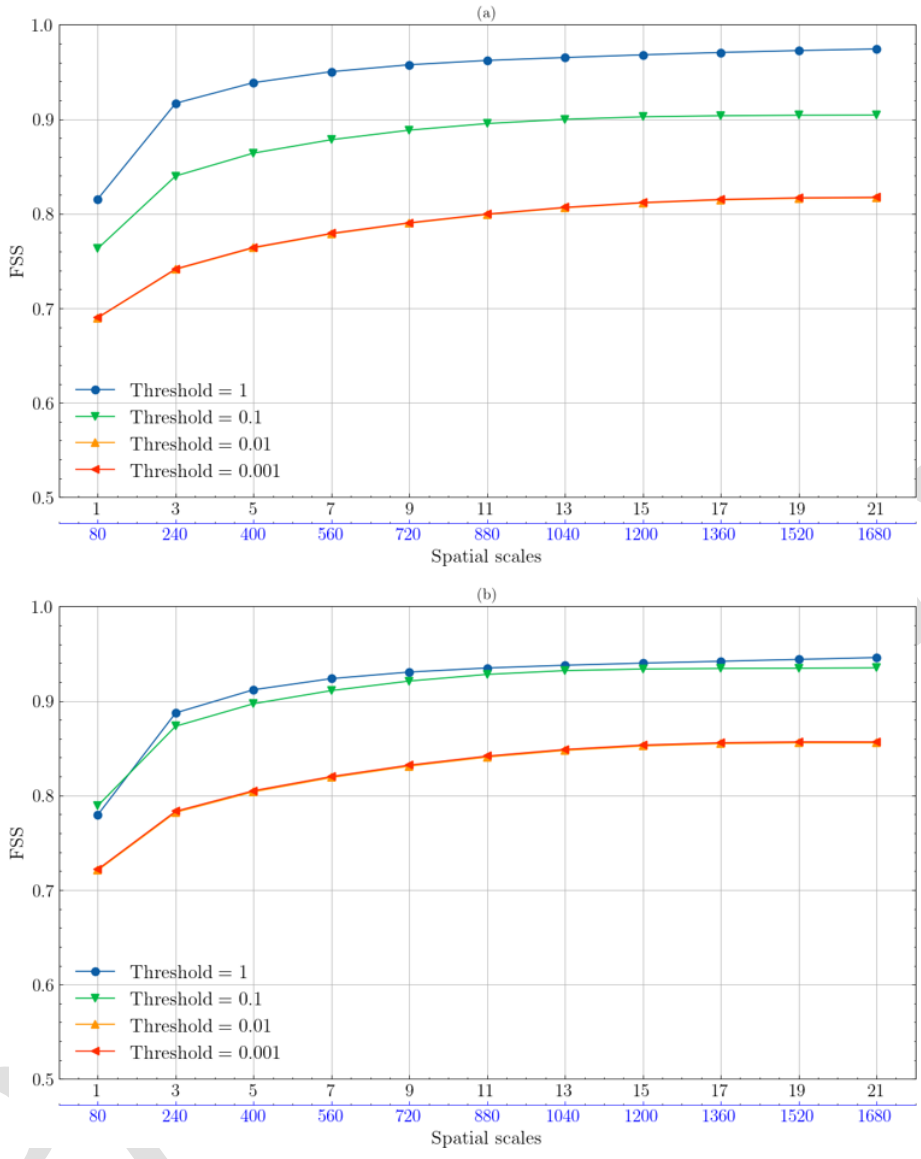


Figure 2. Fraction Skill Score (FSS) as a function of the spatial scale (the number of neighbour cells in black and the distance in meters in blue) for different ranges of firebrand cumulated mass on each cell (thresholds), for the flat terrain (a) and for the hill terrain (b).

tances between 10 and 15 km from the radar location, and falling rain is detected between 25 to 27 km from the radar, as identified by the classes 1, 2 and 5. The plume is bent over and ascends to 4.0 km a.g.l. A small puff appears at a distance of 9.0 km, locally increasing the plume height up to 5.0 km a.g.l. Figure 5b shows a side view of the simulation scalar fields in the atmosphere at 15:44, showing that significant values of instantaneous firebrand mass concentrations (greater than 10^{-5}) reach up to 5.0 km a.g.l. Liquid mixing ratio can be seen at a height of 4.5 km and at a distance of 13 to 15 km from the radar.

Later, at 15:42, in Fig. 6a, rain is identified at 27 to 32 km from the radar location. The plume follows the same initial shape as in Fig. 5a but seems to be falling towards the ground and reaching longitudinal distances of 13.5 km from the radar. Its height reaches up to 5.2 km a.g.l. Figure 6b shows the side view at 16:11. At this stage, firebrand mass concentrations are mainly located in the lower part of the plume, reaching heights of 2.0 km a.g.l. and are transported longitudinally up to a distance of 9.0 km. Liquid mixing ratio is mainly identified at a distance of 26 to 28 km from the radar and at a height of 4.0 to 5.0 km a.g.l.

An approximate description of the plume shape can be obtained by observing the Turbulent Kinetic Energy (TKE) contours. In Fig. 5b, TKE contours, equal to $1.0\,m^2\,s^{-2}$, show that the plume height reaches up to 5.0 km a.g.l., corresponding to the radar observations (Fig. 5a). Laterally, the same contours show a longitudinal extension of the plume

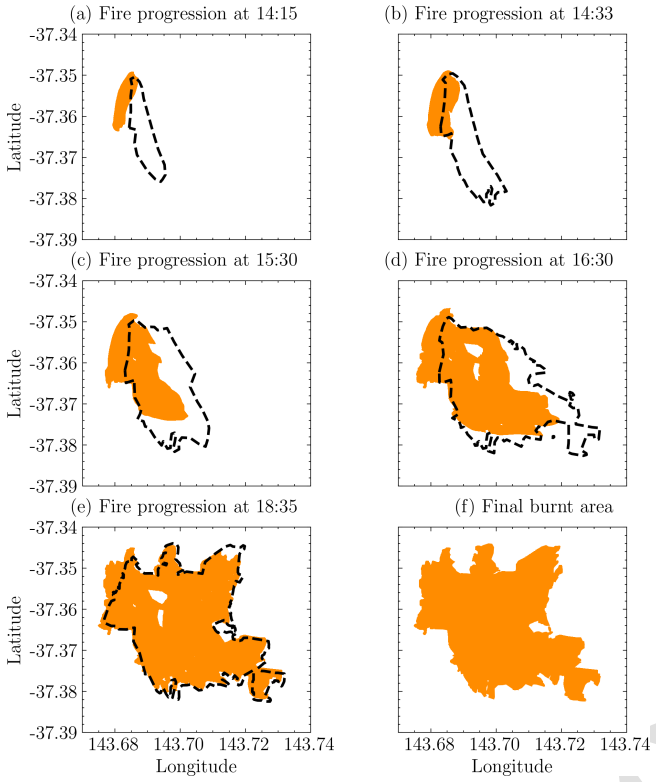


Figure 3. Comparison of actual fire contours as provided by the CFA (in dashed lines) and the simulated fire progression through Meso-NH – ForeFire (orange-coloured contours).



Figure 4. A picture of the plume at 15:40 captured by the CFA ground team (McCarthy et al., 2018).

of approximately 20 km from the radar position, similar to the radar observations (Fig. 5a), where the plume reaches up to 18 km longitudinally. Within the plume, intense updrafts can be identified with closed TKE contours of 3.0 $m^2\ s^{-2}$. In Fig. 6b, the TKE contours of 1.0 $m^2\ s^{-2}$ show that the plume height reaches up to 4.0 km a.g.l. in the second domain, but only 3.0 km a.g.l. in the inner domain. In this case, the simulation shows some differences with respect to the observed plume, where the plume height reaches 5.0 km a.g.l. at a distance of 10 km from the radar position. The simulated plume appears at this point to be more concentrated than the actual observed plume. The TKE contours of 1.0 $m^2\ s^{-2}$ are seen at a distance of 12 to 13 km from the radar, corresponding to the longitudinal extension of the observed plume in Fig. 6a. The detached plume component that is seen at a distance of 20 km from the radar in Fig. 5a, could be reproduced by the 1.0 $m^2\ s^{-2}$ TKE contours that can be seen in Fig. 6b.

Similar snapshots for the simulation performed without the fire can be seen in Fig. 6. In this case, the atmospheric model reproduces well the cloud coverage (see Fig. 4) with liquid mixing ratio values close to 1.0 $g\ kg^{-1}$ at an altitude of 2.5 km a.g.l. and at a distance of 13 km from the radar (Fig. 7a). Similarly, liquid mixing ratio values close to 0.2 $g\ kg^{-1}$ at an altitude of 2.0 km a.g.l. and at a distance of 27 km from the radar location can be seen in Fig. 7b, reproducing the radar observations of Fig. 5a. The influence of the fire on the atmosphere can be seen when comparing Figs. 7a and 5b. Figure 5b shows the presence of clouds at an altitude of 4.5 km a.g.l., whereas the simulation without fire does not show this. TKE contours presented in Fig. 7 show that the convective boundary layer (CBL) height is approximately 2.0 km a.g.l. Whereas in Figs. 5b and 6b, this turbulent mixing layer reaches up to 6.0 a.g.l., indicating the fire-induced overshoot of the CBL.

3.2.3 Firebrand transport

Simulation results for the mass ground deposition are presented in Fig. 8 from 13:15 until 18:15 with an accumulation time of 30 minutes. Observed reported spot fires (individual red dots in the figure) that happened during that same time interval are also included. In Fig. 8, the firebrand mass deposited on the ground is categorized into 5 classes: ranging from 0.01 up to 10.0 kg. These contours represent areas of potential spotting: spatial regions where the deposited firebrand mass is significant.

For the first hour after the fire ignition (13:15), firebrands are deposited south of the fire, following the main wind direction and the plume (Fig. 8a and b). The areas of potential spotting increased as the fire progressed, reaching almost 7 km from the ignition point to the furthest point, where cumulated mass is greater than 0.01 kg (Fig. 8c). At this stage, the shift in the wind was evident in firebrands deposited towards the south-east. During the next time interval, from 15:45 to 15:15 (Fig. 8d), the areas of potential spotting decreased, and the first spot fires were reported during this time interval. All spot fires started within the areas of potential spotting within the previous time interval: from 15:15 to 15:45. Later, the areas of potential spotting shifted towards the east as the fire progressed in that direction. From 15:45 to 16:15 (Fig. 8f), the wind had completed its shift to the west, and the fire progressed towards the east. The areas of potential spotting decreased with respect to the previous time interval. During this time interval, all new reported spot fires also

Not for commercial use only

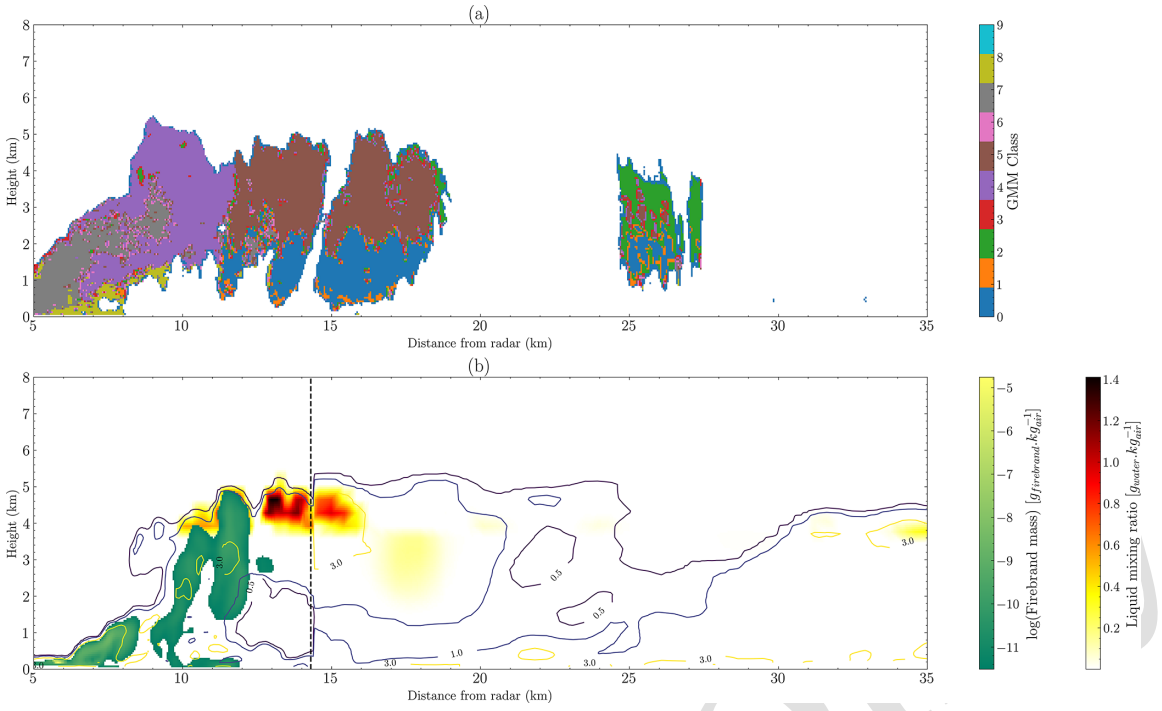


Figure 5. **(a)** Snapshot of the radar echoes GMM segmentation at 15:15, and **(b)** a side view corresponding to the primary RHI scan bearing line with simulation data at 15:44. The dashed line in panel **(b)** corresponds to the limit of the smallest domain. In panel **(b)**, firebrand mass concentrations lower than $5 \times 10^{-3}\,\mathrm{g\,kg^{-1}}$ and liquid mixing ratios lower than $1 \times 10^{-3}\,\mathrm{g\,kg^{-1}}$ were set to NaN values. Contours in panel **(b)** represent isovalues of turbulent kinetic energy for 0.5, 1.0, and $3.0\,\mathrm{m^2\,s^{-2}}$.

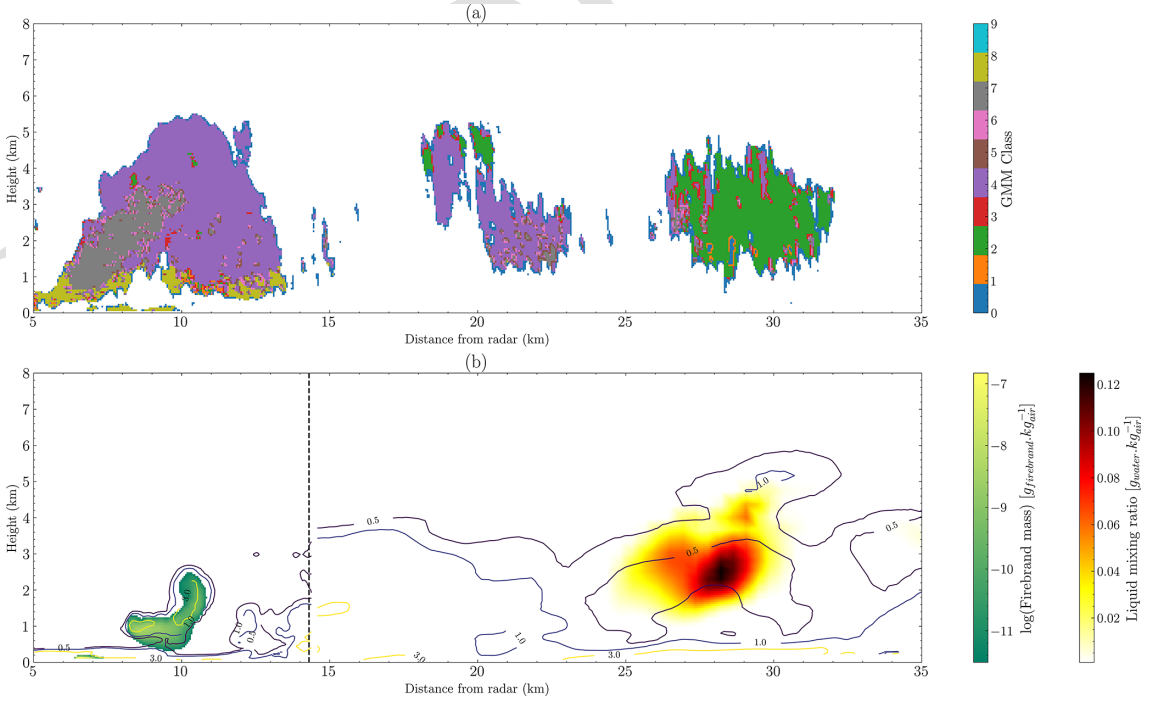


Figure 6. **(a)** Snapshot of the radar echoes GMM class segmentation at 15:42, and **(b)** a side view corresponding to the primary RHI scan bearing line with simulation data at 16 : 11. The dashed line in panel **(b)** corresponds to the limit of the smallest domain. In panel **(b)**, firebrand mass concentrations lower than $5 \times 10^{-3}\,\mathrm{g\,kg^{-1}}$ and liquid mixing ratios lower than $1 \times 10^{-3}\,\mathrm{g\,kg^{-1}}$ were set to *NaN* values. Contours in panel **(b)** represent isovalues of turbulent kinetic energy for 0.5, 1.0, and $3.0\,\mathrm{m^2\,s^{-2}}$.

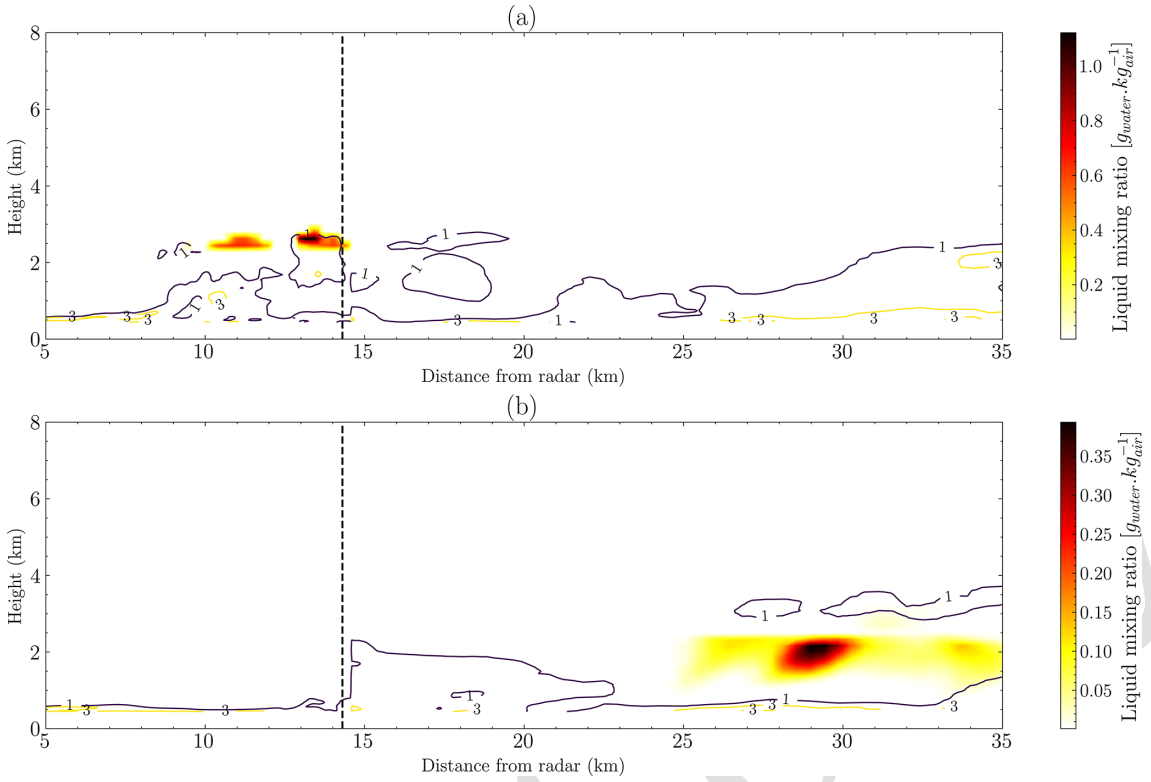


Figure 7. Simulation results of the same side view corresponding to the primary RHI scan bearing line at 15:44 **(a)**, and 16:11 **(b)**. The dashed line corresponds to the limit of the smallest domain. Contours represent isovalues of turbulent kinetic energy for 1.0 and 3.0 $m^2\,s^{-2}$.

started within the simulated areas of potential spotting. From 16:15 to 16:45 (Fig. 8g), fire propagation continues towards the east. Reported spot fires also happened during this time interval and within the potential spotting area. From 16:45 to 17:15 (Fig. 8h), the areas of potential spotting were heavily reduced with respect to the previous time interval, and a large spot fire was reported at 6 km from the main fire front, outside of the simulated potential spotting area. Finally, for the last time interval, Fig. 8i and j show a decrease in the potential spotting areas and no reported spot fires.

Figure 9 presents the temporal evolution of plume top height. The plume top height shows three distinct convective episodes, observed in the simulation, starting at approximately 14:15, 15:15 and 16:15, each reaching heights exceeding 3.0 km a.g.l. The maximum plume is attained at approximately 15:30 with an elevation of 5.6 km a.g.l. Simultaneously, the ratio of the surface area where significant firebrand mass is detected over the injection surface area also shows three local maximums. The apparent increase at the end of the time series results from the rapid decrease in the injection surface area.

3.2.4 Computational performance

In the simulations presented in this study, no specific effort was made to optimize computational performance. A suite of Python scripts was used to construct a coupled Meso-NH – ForeFire simulation based on a given ignition location and date. The spatial extent and resolution of the simulation domains were kept at their default values as defined by the scripts, with no manual modifications applied.

The simulation workflow consists of two main stages. In the first stage, MesoNH is initialized to generate the necessary topographic data, as well as the initial and boundary conditions required for atmospheric forcing. This step also includes a spin-up period to stabilize the model dynamics and can take up to one hour to complete, depending on system performance.

In the second stage, the actual Fire-Atmosphere coupled simulation is executed on a high-performance computing (HPC) system (equipped with Xeon 6230R, 2.1 GHz). The standard simulation was run using 150 CPUs, producing an 8 h fire forecast in approximately 172 min (2.87 h) of wall-clock time. For comparison, an identical atmospheric simulation, without the fire forcing the atmosphere and therefore without calculating the advection and coupling-feedback of fire-related scalar fields, required approximately 143 min. Analysis of computational time showed that the fire-related components of the simulation (fire spread and heat, mass and firebrand flux injection by ForeFire) accounted for 7.8 (%) of the total CPU time in the coupled run, in contrast to 1.2 (%) in

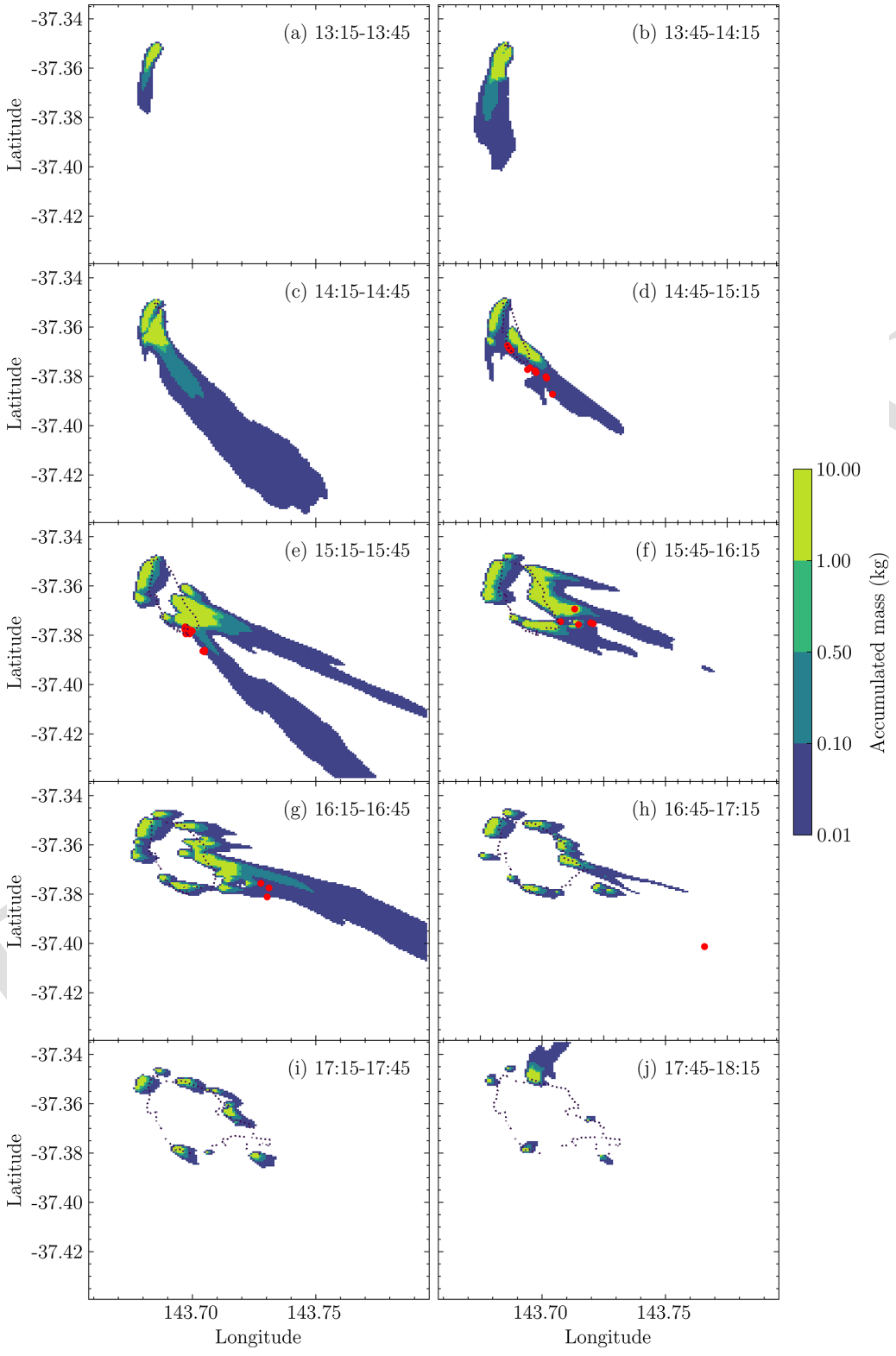


Figure 8. Mass ground densities forecasted by the model during a time interval of 30 min (areas of potential spotting). Red dots represent the spot fires reported by the CFA ground teams. The dotted shape represents the observed fire progression. Firebrand deposition is integrated over the 80 × 80 m cell.

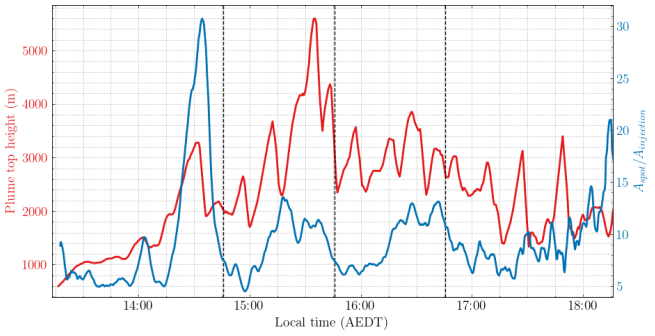


Figure 9. 200 s time averaged, simulation results of the plume top height (red line), defined as the maximum cell height containing at least 0.01 g kg^{-1} of smoke. The blue line shows the fraction of the grid cell surface area containing at least 0.005 g of firebrand mass over the total injection surface area. The dashed lines correspond to end-times given by Fig. 7c, e, and g.

the no-fire atmospheric run. A separate run, using 225 CPUs, reduced the total simulation time to 122 min.

4 Discussion

A Eulerian formulation for spotting was implemented and verified against idealized and realistic wildfire scenarios. Simulation results show good agreement with observed spot fires in terms of spatial and temporal dynamics. The following paragraphs discuss the results obtained and the limitations of the modelling framework.

4.1 Spotting areas

Regarding the idealized cases, the Eulerian model led to similar mass ground landing densities compared to the Lagrangian model. However, it can be seen in Fig. 1a and b that the Eulerian model acted as filter with respect to the Lagrangian results, resulting in a lack of fine details corresponding to individual firebrand landings. This is confirmed by the FSS values from Fig. 2, where the FSS values for lower threshold values (corresponding to low accumulated mass on a given cell), are lower than for higher threshold values. This indicates that the Eulerian model performed worse at low thresholds or few firebrand landings. As it can be seen in Fig. 2, FSS values greater than 0.7 at spatial scales of 3 cell sizes indicate that the Eulerian model reproduces well the Lagrangian results at distances of approximately 240 m. This was also valid across all threshold values, indicating that the Eulerian model reproduces well the ground landing densities at normalized mass values of 0.001.

The two idealized cases also show that the topography plays an important role in the obtained mass ground landing distributions. Although the hill terrain is an idealized representation of a hill with a relatively low height (maximum height of 318 m a.g.l.), its influence on the atmospheric circulations and the final firebrand trajectories was clear. As a result, including the topography in a spotting model would enhance its overall accuracy.

Figure 8a, b and c show that a significant amount of firebrand mass has been deposited on the ground during the first hour and a half since the fire ignition. The potential spotting area, arbitrarily defined here as greater than 0.01 kg, reached a length of almost 13 km in the south-east direction (Fig. 8c). No spot fires were observed or reported by the CFA ground teams during this time interval. However, it is important to acknowledge that unreported extinguishments by landowners may occur, and in some cases, spot fires may spread marginally and self-extinguish without detection. This presents a genuine challenge for comprehensive fire tracking and comparison.

Figure 8d, e, and f illustrate an eastward shift in the burned area and the corresponding potential spotting zones. In this scenario, ignitions occurred within the simulated spotting regions. As shown in Fig. 9g, the locations of reported spot fires largely coincide with the predicted spotting areas. Finally, Fig. 8h highlights a long-range spot fire that was not captured by the simulation during the same time interval (16:45 to 17:15) but is located within the predicted spotting area of the previous time interval (see Fig. 8g).

The results suggest that the current implementation of the model can describe the spatial and temporal dynamics of potential spotting areas with reasonable accuracy but does not accurately determine the occurrence time of spot fires. In fact, the simulation results are approximately 30 min ahead of the observed spot fires: for example, the simulated spotting area in Fig. 8c corresponds more closely to the observed spot fires shown in Fig. 8d, and so on. This discrepancy could be due to a delay between the actual ignition of a spot fire and the time it was reported by ground teams, if reported at all. This delay is uncertain and influenced by several factors, including reflaming of the firebrands, exposure of the firebrand to wind, and the timing of detection by ground teams. It could also be due to a too large terminal velocity that does not accurately describe the firebrand characteristics. Accurately determining the vertical terminal velocity is a key element in the success of the model. The firebrand scalar field will settle at a given terminal velocity and follow a different path compared to the passive tracer, particularly in the presence of a wind shear for example, influencing the deposition zones and the potential spotting areas. Finally, the accuracy of the overall simulation, including fire progression and spot fires' timing, is highly dependent on the boundary conditions used to initialize the simulation.

It should be noted that the fire model is only coupled to MesoNH on the small domain. Accounting for ignitions at distances greater than 15 km would require increasing the domain size, thus increasing computational times, something that could be addressed by using GPU architectures (Escobar et al., 2025). However, the firebrand mass scalar field is still

Proof only

transported within the medium and large domains and could be used to derive potential spotting areas.

Intense convective activity is usually linked to an increase in long-range spotting events and mass spotting events (Castellnou Ribau et al., 2025). This seems to be the case during the Mt Bolton wildfire, with Fig. 9 showing that the simulation captures the link between enhanced convective activity and increased areas of potential spotting. Identifying the time periods when convective activity is likely to intensify could therefore provide valuable support to operational teams responsible for fire control and management.

4.2 Fire and plume behaviour

The observed and simulated fire progression shapes are relatively different at the early stages of the event, but the dynamic behaviour of the simulated fire corresponds to the observed fire behaviour: a progression towards the south followed by a progression towards the east. The fire acceleration during the wind shift is also captured by the simulation as the distance between the fire isochrones decreased. Overall, the simulation seems to be delayed by 30 to 45 min with respect to the actual fire progression. In this case, it is likely that the ERA5 re-analysis has a time shift with respect to the actual wind behaviour, leading to a time difference in terms of fire progression. In this case, it is likely that the ERA5 re-analysis has a time shift with respect to the actual wind behaviour, leading to a time difference in terms of fire progression. TS2 Additionally, although the fire was officially reported to the CFA at 13:45, the simulation was initialized at 13:15 to account for an estimate of the time the fire had been burning prior to detection. This speculation, as the ignition time is unknown, could explain the observed time discrepancy between the simulated fire progression and the observed fire contours. As it can be seen in Fig. 8d, several spot fires happened within the 14:33 perimeter, leading to an increase in the burnt area and an acceleration of the fire front. As a result, modelling reignition could enhance the simulated fire spread dynamics. Finally, we acknowledge that the Rothermel model was developed for, and is typically applied to, Northern Hemisphere coniferous forests which could also explain the differences in fire progression. However, our analysis focuses on ForeFire's performance in spotting transport rather than firebrand generation or forward rate of spread.

The simulation showed a large plume development at three distinct periods: from 14:13 to 14:31; from 14:53 to 15:48; and from 16:06 to 16:25. In the observations, two distinct episodes of intense convection were observed: from 14:33 to 15:15 and from 15:15 to 15:45. Temporally, these observed time intervals are coherent to the simulation results. The westerly wind shift, which happened at approximately 15:02, had an important impact on the final burn area and the spot fire locations. These results confirm the conclusions of Peace et al. (2016), who emphasized the importance of including wind direction changes into operational fire weather forecasts. Overall, the prediction of intense convection activity and the wind shift impact on the fire progression highlight how coupled Fire-Atmosphere models could be suitable in an operational context to provide finer details about the fire behaviour.

As it can be seen in Figs. 4, 5 and 6, the timelapse photographs, radar plume cross section observations, and the simulation are similar in terms of shape, structure and lateral and vertical extent, showing that the simulation reproduces accurately the convective dynamics of the fire. As it can be seen in Fig. 5b, the water content was detected by the radar d at the top of the plume (at a distance of 14 km from the radar and a height of 5 km), but it does not appear in the simulation without fire (Fig. 7a). This indicates that the model was also able to capture the pyroCu development triggered by the pyroconvective activity.

Regarding the dynamics of the injected firebrand mass, the heights reached by the firebrand mass scalar field are also similar with the observed pyrometeors by the radar. Figure 5b shows that a significant firebrand concentration occupied the same space within the plume as the observations. It also shows that a relatively small concentration was found within the same cells occupied by the pyroCu cloud, indicating that simulated firebrands would have passed through the pyroCu. Although it is not possible to attribute specific spot fires to this cluster of firebrands due to the nature of the Eulerian modelling, the observation is in agreement with the study from Lareau (2025), where the author indicated that pyro-meteors were likely to go through the pyroCu/Cb.

4.3 Modelling challenges and future directions

A spotting model, similar to those developed for smoke dispersion (Goodrick et al., 2013), is fundamentally composed of four components: firebrand injection, a plume or advection field description, firebrand transport and fuel bed ignition. In the present study, the final ignition component was deliberately excluded, with the primary focus placed on integrating the injection and transport processes within a coupled Fire-Atmosphere framework.

The firebrand injection component remains one of the most challenging to model with physical realism because of the lack of experimental data and observations. Injection should capture the variability of firebrand size, shape and density, as well as the firebrand production rates as functions of vegetation type, fire behaviour, and atmospheric conditions (Ju et al., 2023; Wickramasinghe et al., 2022). In this work, a simplified injection scheme was employed using a constant firebrand mass flux over a prescribed injection duration. While numerically efficient, this approach neglects possible dependencies of injected mass on fire intensity, wind velocity, and fuel characteristics. Future experimental work is required to better characterize this first component, in-

Proof only

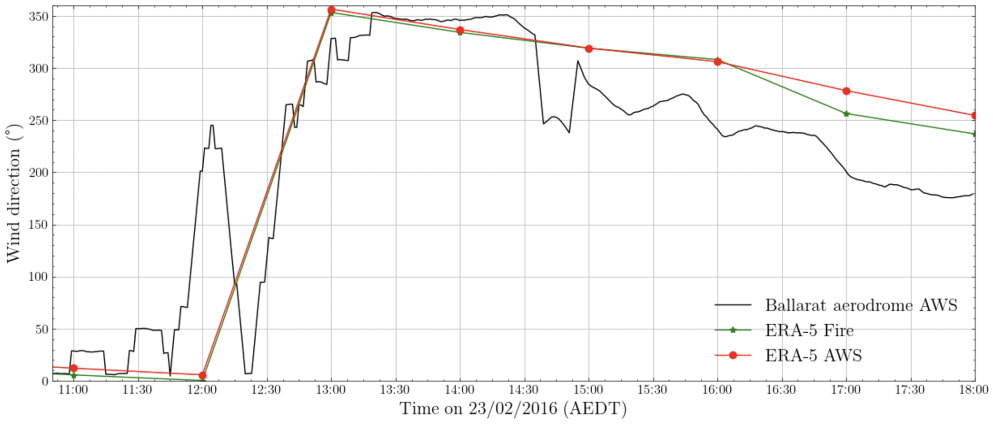


Figure 10. Horizontal wind direction as a function of the local time for the AWS located in the Ballarat aerodrome, using ERA5 data at the same location and using ERA5 data at the bushfire ignition location. The plotted AWS data is the 10 min moving average calculated from a 1 min sampling signal.

creasing the realism of the simulations and improving the predictive skill of the model.

The representation of plume dynamics and overall Fire-Atmosphere interactions was modelled using a coupled Fire–Atmosphere framework, which is a key strength of this study. Previous work has demonstrated the capability of such models to resolve buoyancy-driven plume rise and turbulent entrainment (Baggio et al., 2022; Couto et al., 2024; Kochanski et al., 2013; Peace et al., 2023, 2022, 2015). This simulation framework, following similar approach as Kepert et al. (2024), addresses the challenge highlighted by Storey et al. (2020): existing spotting models are not adapted to extreme fires because they do not account for "highly convective plumes or large aerodynamic firebrands". The comparison to Radar data shows that the model reproduces well the plume height, the plume longitudinal extent and the local weather processes leading to the generation of a PyroCu. This provides a physically consistent advection field in which to embed firebrand transport and is a major advantage over models relying on prescribed wind fields or static plume shapes. The success of this component highlights the value of integrating firebrand transport within dynamically evolving fire simulations (Thurston et al., 2017). Further efforts should be dedicated to comparing wind fields from observational data.

The third component involves the transport of firebrands through the atmosphere, and the results presented here show that this step could be done simultaneously with plume evolution. However, a key limitation lies in the scarcity of experimental data on medium- to long-range spotting, complicating the validation process. Incorporating combustion-phase transitions (flaming to smouldering) was outside of the scope of this work. Yet, including the combustion process as a mass reduction dependent on environmental variables (wind, turbulent kinetic energy) could effectively reduce the overall mass transported and decrease the potential spotting areas, increasing the predictive accuracy of the model. Including such a process would enable finer control over where and when spotting can occur, particularly important when parametrizing the re-ignition process.

The Eulerian approach to firebrand transport, while computationally efficient, introduces a filtering effect that smooths out finer features captured by Lagrangian particle-based models. It omits stochastic variability in particle motion, especially relevant in regions of strong turbulence. The current implementation assumes a constant terminal velocity and ignores size-dependent particle dynamics. A more physically realistic formulation of terminal velocity (Thomas et al., 2020), would improve predictions of firebrand landing patterns. Likewise, the assumption of ground-level injection does not reflect observed high-elevation firebrand releases during crowning events (Albini et al., 2012), which can increase potential transport distances. Future models could benefit from distributed vertical injection profiles informed by flame height and fire structure.

Firebrand transport was modelled using a scalar advection equation. This assumption may be overly conservative. Due to their inertia, large firebrands (denser than air) do not follow the smallest turbulent eddies but rather respond to the larger turbulent structures. This suggests that the scalar diffusivity for firebrands should be greater than that of a passive tracer. Following pollen dispersion studies (Dupont et al., 2006), assigning a Schmidt number (Sc) less than unity ($Sc = 0.6$) would better capture this enhanced dispersion.

Finally, the last component of a spotting model is the firebrand deposition and ignition of fuels. Firebrands can be deposited at different vertical layers of the vegetation (ground, surface or aerial), and their accumulation also plays an important role in fuel ignition (Suzuki and Manzello, 2020), making this final process challenging to model. The solution proposed by Frediani et al. (2025) suggest using two user-defined thresholds: one applied to the firebrand deposi-

Proof only

tion within a given numerical cell and another related to the number of neighbouring cells receiving firebrands required to trigger a spot ignition. Although this solution is interesting to account for spatial coherence, we hypothesise that a stochastic ignition with a lower and upper (to limit the number of ignitions near the firebrand injection area) threshold might add physical realism to the simulations.

While subject to several assumptions and potential improvements, the results support the potential for operational purposes of MesoNH-ForeFire. Obtaining an 8 h forecast in approximately 3 h can be of great interest to determine fire progression and potential spotting areas. Regarding spotting, some possibilities of this kind of modelling include: providing spatial information to monitor areas that could be ignited by firebrands, providing temporal information regarding the potential spot fires occurrence, and early warning systems for wildland-urban interface fires to alert citizens.

This study also highlights the importance of high-resolution weather radar data for model evaluation and interpretation, as frequency of observations (seconds to minute) and spatial resolution (tens of metres voxels) are comparable to the coupled Fire-Atmosphere model outputs. At present, such high-resolution datasets are scarce, as dedicated portable weather radar has to be deployed near the fireground, minutes after the fire has been reported, and only a few research groups in the US and Australia have that capacity. However, fire agencies are showing interest in deploying such tools within operations, which would lead to a substantial increase of high-quality dataset for model evaluation in the future.

5 Conclusion

This study presents a Eulerian modelling approach for simulating medium and long-distance spotting within a coupled Fire-Atmosphere framework. The model was evaluated through both idealized and realistic case studies to assess its potential applicability in an operational wildfire forecasting system. Results indicate that the proposed model can describe accurately the spatiotemporal dynamics of spotting while maintaining a high degree of numerical efficiency.

In the idealized simulations, the Eulerian model produced ground firebrand deposition patterns comparable to those obtained using a Lagrangian formulation, particularly at spatial resolutions on the order of 200 to 400 m. Key results showed that the model was able to identify potential spotting areas with acceptable temporal accuracy offering useful insights for real-time fire management. In the case of the Mt Bolton wildfire, the model reproduced the intensity and timing of observed spotting events with good qualitative agreement, underscoring its potential in operational utilisation.

Some limitations of this study mainly include a simplified representation of the firebrand dynamics, specifically the use of a single terminal settling velocity that does not account for the heterogeneous characteristics of firebrands (e.g., shape, mass, combustion state). While this simplification enhances computational efficiency, it may limit the physical realism of the model under diverse wildfire conditions.

Future research should focus on refining the Eulerian formulation by incorporating turbulence-driven dispersion mechanisms into the mass scalar field, improving firebrand injection parameterizations based on experimental data or inverse modelling techniques, and refining the fuel bed ignition model to better represent spot ignition processes. Additionally, the model should be tested against a broader range of wildfire events, both within Australia and in other fire-prone regions, to evaluate its robustness across different vegetation types, topographies and meteorological conditions.

Overall, the results confirm the viability of the Eulerian formulation in an operational context. This modelling framework can improve fire spread models and enhance wildfire management strategies.

Data availability. Files required for the simulation of the Mt Bolton wildfire can be found at https://doi.org/10.5281/zenodo.17241970 (Alonso Pinar, 2025). Required software can be found in https://src.koda.cnrs.fr/jean.baptiste.filippi/meso-nh-fire-code (last access: 19 November 2026) (commit 5fe710ff) and https://doi.org/10.21105/joss.08680 (Filippi et al., 2025) (commit e2e959a).

Author contributions. AAP performed the LES simulations and subsequent analysis and wrote the paper. JBF set up the initial setup of the simulations and postprocessing of simulation files and provided regular feedback on the ongoing analysis and paper writing. AAP and JBF developed the firebrand Eulerian injection, transport and deposition in MesoNH-ForeFire. AG analysed radar data and performed the segmentation of polarimetric radar data. NM participated in the Mt Bolton campaign and collected radar data and spotting location and timestamps. PT helped with the setup of the Eulerian model in MesoNH. Finally, AF helped to develop the firebrand injection mechanism and provided regular feedback on the manuscript. All authors assisted with the conceptualisation of the research and acted as internal reviewers by correcting the manuscript.

Competing interests. The contact author has declared that none of the authors has any competing interests.

Disclaimer. Publisher's note: Copernicus Publications remains neutral with regard to jurisdictional claims made in the text, published maps, institutional affiliations, or any other geographical representation in this paper. The authors bear the ultimate responsibility for providing appropriate place names. Views expressed in the text are those of the authors and do not necessarily reflect the views of the publisher.

Proof only

Acknowledgements. This research was supported by the computational resources of the Université de Corse, and by The University of Melbourne's Research Computing Services and the Petascale Campus Initiative. This project was undertaken with the assistance of resources from the Australian National Computational Infrastructure (NCI) and the Australian Bureau of Meteorology, both of which are supported by the Australian Government. The open-source libraries NumPy (van der Walt et al., 2011), SciPy (Virtanen et al., 2020), Matplotlib (Hunter, 2007), netCDF4 (Rew and Davis, 1990), and scikit-learn (Pedregosa et al., 2011) in the Python programming language (Rossum, 1995) were used to develop and implement the code to process the data.

Financial support. Alberto Alonso Pinar was funded by the Graduate Research Projects Scheme between the Centre National de la Recherche Scientifique and The University of Melbourne, "Multiscale experimentation and simulation of wildfire SPOTting". Alex Filkov was supported by the Research into Building Performance during Bush Fires (RFS4) project, funded by the New South Wales Rural Fire Service. Jean Baptiste Filippi was supported by EU's H2020 101037419 Fire-Res program. Adrien Guyot was supported by Google.org, Google's philanthropic organisation (grant no. TF2103-098173).

Review statement. This paper was edited by Ricardo Trigo and reviewed by Akli Benali and one anonymous referee.

References

Albini, F. A.: Spot fire distance from burning trees: a predictive model, USDA Forest Service, Intermountain Forest and Range Experiment Station 73, https://www.frames.gov/catalog/8153 (last access: 19 November 2026), 1979.

Albini, F. A.: Spot Fire Distance from Isolated Sources: Extensions of a Predictive Model, USDA Forest Service, Intermountain Forest and Range Experiment Station, https://agris.fao.org/search/en/providers/122535/records/65ddd4e90f3e94b9e5c57f72 (last access: 19 November 2026), 1981.

Albini, F. A.: Transport of Firebrands by Line Thermals, Combust. Sci. Technol., 32, 277–288, https://doi.org/10.1080/00102208308923662, 1983.

Albini, F. A., Alexander, M. E., and Cruz, M. G.: A mathematical model for predicting the maximum potential spotting distance from a crown fire, Int. J. Wildland Fire, 21, 609–627, https://doi.org/10.1071/WF11020, 2012.

Alonso Pinar, A.: Simulation files for Eulerian modelling of spotting using a coupled Fire-Atmosphere approach, Zenodo [data set], https://doi.org/10.5281/zenodo.17241970, 2025.

Alonso-Pinar, A., Filippi, J.-B., and Filkov, A.: Modelling aerodynamics and combustion of firebrands in long-range spotting, Fire Safety J., 152, https://doi.org/10.1016/j.firesaf.2025.104348, 2025a.

Alonso-Pinar, A., Filippi, J.-B., Nguyen, H.-N., and Filkov, A.: A simplified model to incorporate firebrand transport into coupled fire atmosphere models, Int. J. Wildland Fire, 34, https://doi.org/10.1071/wf24200, 2025b.

Anand, C., Shotorban, B., and Mahalingam, S.: Dispersion and deposition of firebrands in a turbulent boundary layer, Int. J. Multiphas. Flow, 109, 98–113, https://doi.org/10.1016/j.ijmultiphaseflow.2018.07.012, 2018.

Baggio, R., Filippi, J. B., Truchot, B., and Couto, F. T.: Local to continental scale coupled fire-atmosphere simulation of large industrial fire plume, Fire Safety J., 134, 103699, https://doi.org/10.1016/j.firesaf.2022.103699, 2022.

Barr, B. W. and Ezekoye, O. A.: Thermo-mechanical modeling of firebrand breakage on a fractal tree, P. Combust. Inst., 34, 2649–2656, https://doi.org/10.1016/j.proci.2012.07.066, 2013.

Bhutia, S., Jenkins, M. A., and Sun, R.: Comparison of firebrand propagation prediction by a plume model and a coupled-fire/atmosphere large-eddy simulator, J. Adv. Model. Earth Sy., 2, 4, https://doi.org/10.3894/JAMES.2010.2.4, 2010.

Bougeault, P. and Lacarrere, P.: Parameterization of Orography-Induced Turbulence in a Mesobeta–Scale Model, Mon. Weather Rev., 117, 1872–1890, https://doi.org/10.1175/1520-0493(1989)117<1872:POOITI>2.0.CO;2, 1989.

Caniaux, G., Redelsperger, J.-L., and Lafore, J.-P.: A Numerical Study of the Stratiform Region of a Fast-Moving Squall Line. Part I: General Description and Water and Heat Budgets, J. Atmos. Sci., 51, 2046–2074, https://doi.org/10.1175/1520-0469(1994)051<2046:ANSOTS>2.0.CO;2, 1994.

Castellnou Ribau, M., Bachfischer, M., Guarque, P., Estivill, L., Miralles Bover, M., Ruiz, B., Pagès, J., Verhoeven, B., Ntasiou, Z., Stokkeland, O., van Heerwaarden, C., Roelofs, T., Janssens, M., Stoof, C. R., and Vilà-Guerau de Arellano, J.: Integrating fireline observations to characterize fire plumes during pyroconvective extreme wildfire events: implications for firefighter safety and plume modeling, Atmos. Meas. Tech., 18, 7805–7831, https://doi.org/10.5194/amt-18-7805-2025, 2025.

Cervantes, A. Q.: Numerical Modeling of Firebrand Transport, MSc thesis, San Jose State University, San Jose, CA, USA, https://doi.org/10.31979/etd.ddm6-vzya, 2023.

Colella, P. and Woodward, P. R.: The Piecewise Parabolic Method (PPM) for gas-dynamical simulations, J. Comput. Phys., 54, 174–201, https://doi.org/10.1016/0021-9991(84)90143-8, 1984.

Costa, A., Macedonio, G., and Folch, A.: A three-dimensional Eulerian model for transport and deposition of volcanic ashes, Earth Planet. Sc. Lett., 241, 634–647, https://doi.org/10.1016/j.epsl.2005.11.019, 2006.

Couto, F. T., Filippi, J.-B., Baggio, R., Campos, C., and Salgado, R.: Numerical investigation of the Pedrógão Grande pyrocumulonimbus using a fire to atmosphere coupled model, Atmos. Res., 299, 107223, https://doi.org/10.1016/j.atmosres.2024.107223, 2024.

Cruz, M. G., Gould, J. S., Alexander, M. E., Sullivan, A. L., McCaw, W. L., and Matthews, S.: A guide to rate of fire spread models for Australian vegetation, Australasian Fire and Emergency Service Authorities Council Ltd and Commonwealth Scientific and Industrial Research Organisation, East Melbourne, Victoria, ISBN: 978-0-9872065-4-1, 2015.

Cuxart, J., Bougeault, P., and Redelsperger, J.-L.: A turbulence scheme allowing for mesoscale and large-eddy simulations, Q. J. Roy. Meteor. Soc., 126, 1–30, https://doi.org/10.1002/qj.49712656202, 2000.

Dupont, S., Brunet, Y., and Jarosz, N.: Eulerian modelling of pollen dispersal over heterogeneous vege-

Proof Only

tation canopies, Agr. Forest Meteorol., 141, 82–104, https://doi.org/10.1016/j.agrformet.2006.09.004, 2006.

Escobar, J., Wautelet, P., Pianezze, J., Pantillon, F., Dauhut, T., Barthe, C., and Chaboureau, J.-P.: Porting the Meso-NH atmospheric model on different GPU architectures for the next generation of supercomputers (version MESONH-v55-OpenACC), Geosci. Model Dev., 18, 2679–2700, https://doi.org/10.5194/gmd-18-2679-2025, 2025.

Filippi, J. B., Bosseur, F., Mari, C., Lac, C., Le Moigne, P., Cuenot, B., Veynante, D., Cariolle, D., and Balbi, J.: Coupled Atmosphere-Wildland Fire Modelling, J. Adv. Model. Earth Sy., 1, 4, https://doi.org/10.3894/JAMES.2009.1.11, 2009.

Filippi, J.-B., Bosseur, F., Pialat, X., Santoni, P.-A., Strada, S., and Mari, C.: Simulation of Coupled Fire/Atmosphere Interaction with the MesoNH-ForeFire Models, J. Combust., 540390, https://doi.org/10.1155/2011/540390, 2011.

Filippi, J.-B., Pialat, X., and Clements, C. B.: Assessment of ForeFire/Meso-NH for wildland fire/atmosphere coupled simulation of the FireFlux experiment, P. Combust. Inst., 34, 2633–2640, https://doi.org/10.1016/j.proci.2012.07.022, 2013.

Filippi, J.-B., Bosseur, F., Mari, C., and Lac, C.: Simulation of a Large Wildfire in a Coupled Fire-Atmosphere Model, Atmosphere, 9, 218, https://doi.org/10.3390/atmos9060218, 2018.

Filippi, J.-B., Baggio, R., Paugam, R., Bosseur, F., Leblanc, A., and Alonso-Pinar, A.: ForeFire: A Modular, Scriptable C++ Simulation Engine and Library for Wildland-Fire Spread, Journal of Open Source Software, 10, 8680, https://doi.org/10.21105/joss.08680, 2025.

Filkov, A., Prohanov, S., Mueller, E., Kasymov, D., Martynov, P., Houssami, M. E., Thomas, J., Skowronski, N., Butler, B., Gallagher, M., Clark, K., Mell, W., Kremens, R., Hadden, R. M., and Simeoni, A.: Investigation of firebrand production during prescribed fires conducted in a pine forest, P. Combust. Inst., 36, 3263–3270, https://doi.org/10.1016/j.proci.2016.06.125, 2017.

Frediani, M., Shamsaei, K., Juliano, T. W., Ebrahimian, H., Kosović, B., Knievel, J. C., and Tessendorf, S. A.: Modeling Firebrand Spotting in WRF-Fire for Coupled Fire–Weather Prediction, Fire, 8, 374, https://doi.org/10.3390/fire8100374, 2025.

Goodrick, S. L., Achtemeier, G. L., Larkin, N. K., Liu, Y., and Strand, T. M.: Modelling smoke transport from wildland fires: a review, Int. J. Wildland Fire, 22, 83–94, https://doi.org/10.1071/WF11116, 2013.

Guyot, A., Brook, J. P., Protat, A., Turner, K., Soderholm, J., McCarthy, N. F., and McGowan, H.: Segmentation of polarimetric radar imagery using statistical texture, Atmos. Meas. Tech., 16, 4571–4588, https://doi.org/10.5194/amt-16-4571-2023, 2023.

Haider, A. and Levenspiel, O.: Drag coefficient and terminal velocity of spherical and nonspherical particles, Powder Technol., 58, 63–70, https://doi.org/10.1016/0032-5910(89)80008-7, 1989.

Hersbach, H., Bell, B., Berrisford, P., Biavati, G., Horányi, A., Muñoz Sabater, J., Nicolas, J., Peubey, R., Radu, R., Rozum, I., Schepers, D., Simmons, A., Soci, C., Dee, D., and Thépaut, J.-N.: ERA5 hourly data on single levels from 1940 to present, Copernicus Climate Change Service (C3S) Climate Data Store (CDS) [data set], https://doi.org/10.24381/CDS.ADBB2D47, 2023.

Himoto, K. and Tanaka, T.: Transport of disk-shaped firebrands in a turbulent boundary layer, Fire Safety Sci., 8, 433–444, https://publications.iafss.org/publications/fss/8/433 (last access: 19 November 2026), 2005.

Hunter, J. D.: Matplotlib: A 2D graphics environment, Comput. Sci. Eng., 9, 90–95, https://doi.org/10.1109/MCSE.2007.55, 2007.

Ju, X., Conkling, M., Hajilou, M., Lin, S., Mostafa, F., Ayyar, A., McDowell, A., Lisano, M., and Gollner, M. J.: Laboratory quantification of firebrand generation from WUI fuels for model development, Fire Safety J., 141, 103921, https://doi.org/10.1016/j.firesaf.2023.103921, 2023.

Kepert, J. D., Thurston, W., and Tory, K. J.: A fast, physically based model of firebrand transport by bushfire plumes, Agr. Forest Meteorol., 345, 109839, https://doi.org/10.1016/j.agrformet.2023.109839, 2024.

Kochanski, A. K., Krueger, S. K., Jenkins, M. A., Mandel, J., and Beezley, J. D.: Coupled Atmosphere-Fire Simulations of Fireflux: Impacts of Model Resolution on Model Performance, arXiv [preprint], https://doi.org/10.48550/arXiv.1112.0494, 2011.

Kochanski, A. K., Jenkins, M. A., Mandel, J., Beezley, J. D., Clements, C. B., and Krueger, S.: Evaluation of WRF-SFIRE performance with field observations from the FireFlux experiment, Geosci. Model Dev., 6, 1109–1126, https://doi.org/10.5194/gmd-6-1109-2013, 2013.

Kochanski, A. K., Jenkins, M. A., Yedinak, K., Mandel, J., Beezley, J. D., and Lamb, B.: Toward an integrated system for fire, smoke, and air quality simulations, Int. J. Wildland Fire, 25, 534–546, https://doi.org/10.1071/WF14074, 2016.

Kochanski, A.K., Herron-Thorpe, F., Mallia, D.V., Mandel, J., and Vaughan, J.K.: Integration of a coupled fire-atmosphere model into a regional air quality forecasting system for wildfire events, Front. For. Glob. Change, 4, 728726, https://doi.org/10.3389/ffgc.2021.728726, 2021.

Koo, E., Pagni, P. J., Weise, D. R., and Woycheese, J. P.: Firebrands and spotting ignition in large-scale fires, Int. J. Wildland Fire, 19, 818–843, https://doi.org/10.1071/WF07119, 2010.

Lac, C., Chaboureau, J.-P., Masson, V., Pinty, J.-P., Tulet, P., Escobar, J., Leriche, M., Barthe, C., Aouizerats, B., Augros, C., Aumond, P., Auguste, F., Bechtold, P., Berthet, S., Bielli, S., Bosseur, F., Caumont, O., Cohard, J.-M., Colin, J., Couvreux, F., Cuxart, J., Delautier, G., Dauhut, T., Ducrocq, V., Filippi, J.-B., Gazen, D., Geoffroy, O., Gheusi, F., Honnert, R., Lafore, J.-P., Lebeaupin Brossier, C., Libois, Q., Lunet, T., Mari, C., Maric, T., Mascart, P., Mogé, M., Molinié, G., Nuissier, O., Pantillon, F., Peyrillé, P., Pergaud, J., Perraud, E., Pianezze, J., Redelsperger, J.-L., Ricard, D., Richard, E., Riette, S., Rodier, Q., Schoetter, R., Seyfried, L., Stein, J., Suhre, K., Taufour, M., Thouron, O., Turner, S., Verrelle, A., Vié, B., Visentin, F., Vionnet, V., and Wautelet, P.: Overview of the Meso-NH model version 5.4 and its applications, Geosci. Model Dev., 11, 1929–1969, https://doi.org/10.5194/gmd-11-1929-2018, 2018.

Lafore, J. P., Stein, J., Asencio, N., Bougeault, P., Ducrocq, V., Duron, J., Fischer, C., Héreil, P., Mascart, P., Masson, V., Pinty, J. P., Redelsperger, J. L., Richard, E., and Vilà-Guerau de Arellano, J.: The Meso-NH Atmospheric Simulation System. Part I: adiabatic formulation and control simulations, Ann. Geophys., 16, 90–109, https://doi.org/10.1007/s00585-997-0090-6, 1998.

Lareau, N. P.: Plume Dynamics Drive Extreme Long-Range Spotting During California's Dixie Fire, J. Geophys. Res.-Atmos., 130, e2024JD043167, https://doi.org/10.1029/2024JD043167, 2025.

López-De-Castro, M., Trucchia, A., Morra Di Cella, U., Fiorucci, P., Cardillo, A., and Pagnini, G.: Fire-spotting modelling in

Proof Only

operational wildfire simulators based on Cellular Automata: A comparison study, Agr. Forest Meteorol., 350, 109989, https://doi.org/10.1016/j.agrformet.2024.109989, 2024.

McCarthy, N., McGowan, H., Guyot, A., and Dowdy, A.: Mobile X-Pol Radar: a new tool for investigating pyroconvection and associated wildfire meteorology, B. Am. Meteorol. Soc., 99, 1177–1195, https://doi.org/10.1175/bams-d-16-0118.1, 2018.

McCarthy, N. F., Guyot, A., Protat, A., Dowdy, A. J., and McGowan, H.: Tracking pyrometeors with meteorological radar using unsupervised machine learning, Geophys. Res. Lett., 47, e2019GL084305, https://doi.org/10.1029/2019GL084305, 2020.

Noble, I. R., Gill, A. M., and Bary, G. A. V.: McArthur's fire-danger meters expressed as equations, Aust. J. Ecol., 5, 201–203, https://doi.org/10.1111/j.1442-9993.1980.tb01243.x, 1980.

Oliveira, L. A., Lopes, A. G., Baliga, B. R., Almeida, M., and Viegas, D. X.: Numerical prediction of size, mass, temperature and trajectory of cylindrical wind-driven firebrands, Int. J. Wildland Fire, 23, 698–708, https://doi.org/10.1071/WF13080, 2014.

Peace, M., Mattner, T., Mills, G., Kepert, J., and McCaw, L.: Fire-Modified Meteorology in a Coupled Fire–Atmosphere Model, J. Appl. Meteorol. Clim., 54, 704–720, https://doi.org/10.1175/JAMC-D-14-0063.1, 2015.

Peace, M., Mattner, T., Mills, G., Kepert, J., and McCaw, L.: Coupled Fire–Atmosphere Simulations of the Rocky River Fire Using WRF-SFIRE, J. Appl. Meteorol. Clim., 55, 1151–1168, https://doi.org/10.1175/JAMC-D-15-0157.1, 2016.

Peace, M., Greenslade, J., Ye, H., and Kepert, J. D.: Simulations of the Waroona fire using the coupled atmosphere–fire model ACCESS-Fire, J. South. Hemisph. Earth Syst. Sci., 72, 126–138, https://doi.org/10.1071/ES22013, 2022.

Peace, M., Ye, H., Greenslade, J., and Kepert, J. D.: The Destructive Sir Ivan Fire in New South Wales, Australia; Simulations Using a Coupled Fire-Atmosphere Model, Fire, 6, 438, https://doi.org/10.3390/fire6110438, 2023.

Pedregosa, F., Varoquaux, G., Gramfort, A., Michel, V., Thirion, B., Grisel, O., Blondel, M., Prettenhofer, P., Weiss, R., Dubourg, V., Vanderplas, J., Passos, A., Cournapeau, D., Brucher, M., Perrot, M., and Duchesnay, E.: Scikit-learn: Machine learning in Python, J. Mach. Learn. Res., 12, 2825–2830, 2011.

Pinty, J.-P., Cosma, S., Cohard, J.-M., Richard, E., and Chaboureau, J.-P.: CCN sensitivity of a warm precipitation event over fine scale orography with an advanced microphysical scheme, Atmos. Res., 59–60, 419–446, https://doi.org/10.1016/S0169-8095(01)00128-4, 2001.

Qin, Y. and Trouvé, A.: A numerically accurate mathematical framework for simulations of firebrand transport in landscape-scale fire spread models, Fire Safety J., 152, 104343, https://doi.org/10.1016/j.firesaf.2025.104343, 2025.

Rew, R. and Davis, G.: NetCDF: an interface for scientific data access, IEEE Comput. Graph.,10, 76–82, https://doi.org/10.1109/38.56302, 1990.

Roberts, N. M. and Lean, H. W.: Scale-Selective Verification of Rainfall Accumulations from High-Resolution Forecasts of Convective Events, Mon. Weather Rev., 136, 78–97, https://doi.org/10.1175/2007MWR2123.1, 2008.

Rossum, G.: Python reference manual, Centre for Mathematics and Computer Science, https://dl.acm.org/doi/abs/10.5555/869369 (last access: 19 November 2026), 1995.

Rothermel, R.: A mathematical model for predicting fire spread in wildland fuels, Intermountain Forest & Range Experiment Station, Forest Service, US Department of Agriculture, Ogden, Research Paper INT-115, https://doi.org/10.2737/INT-RP-115, 1972.

Sardoy, N., Consalvi, J., Porterie, B., and Fernandez-Pello, A.: Modeling transport and combustion of firebrands from burning trees, Combust. Flame, 150, 151–169, https://doi.org/10.1016/j.combustflame.2007.04.008, 2007.

Sardoy, N., Consalvi, J. L., Kaiss, A., Fernandez-Pello, A. C., and Porterie, B.: Numerical study of ground-level distribution of firebrands generated by line fires, Combust. Flame, 154, 478–488, https://doi.org/10.1016/j.combustflame.2008.05.006, 2008.

Simpson, C. C., Sharples, J. J., Evans, J. P., and McCabe, M. F.: Large eddy simulation of atypical wildland fire spread on leeward slopes, Int. J. Wildland Fire, 22, 599–614, https://doi.org/10.1071/WF12072, 2013.

Simpson, C. C., Sharples, J. J., and Evans, J. P.: Resolving vorticity-driven lateral fire spread using the WRF-Fire coupled atmosphere–fire numerical model, Nat. Hazards Earth Syst. Sci., 14, 2359–2371, https://doi.org/10.5194/nhess-14-2359-2014, 2014.

Skamarock, W. C.: Positive-Definite and Monotonic Limiters for Unrestricted-Time-Step Transport Schemes, Mon. Weather Rev., 134, 2241–2250, https://doi.org/10.1175/MWR3170.1, 2006.

Soderholm, J., McGowan, H., Richter, H., Walsh, K., Weckwerth, T., and Coleman, M.: The Coastal Convective Interactions Experiment (CCIE): Understanding the Role of Sea Breezes for Hailstorm Hotspots in Eastern Australia, B. Am. Meteorol. Soc., 97, 1687–1698, https://doi.org/10.1175/BAMS-D-14-00212.1, 2016.

Storey, M. A., Price, O. F., Sharples, J. J., and Bradstock, R. A.: Drivers of long-distance spotting during wildfires in south-eastern Australia, Int. J. Wildland Fire, 29, 459–472, https://doi.org/10.1071/WF19124, 2020.

Sullivan, A. L.: Wildland surface fire spread modelling, 1990–2007. 1: Physical and quasi-physical models, Int. J. Wildland Fire, 18, 349–368, https://doi.org/10.1071/WF06143, 2009.

Suzuki, S. and Manzello, S. L.: Role of accumulation for ignition of fuel beds by firebrands, Appl. Energ. Combust. Sci., 1–4, 100002, https://doi.org/10.1016/j.jaecs.2020.100002, 2020.

Tarifa, C. S., del Notario, P. P., and Moreno, F. G.: On the flight paths and lifetimes of burning particles of wood, Int. Symp. on Comb., 10, 1021–1037, https://doi.org/10.1016/S0082-0784(65)80244-2, 1965.

Tarifa, C. S., del Notario, P. P., and Moreno, F. G.: Transport and combustion of firebrands, Instituto Nacional de Técnica Aeroespacial, https://oa.upm.es/6521/ (last access: 19 November 2026), 1967.

Thomas, C. M., Sharples, J. J., and Evans, J. P.: Modelling the dynamic behaviour of junction fires with a coupled atmosphere–fire model, Int. J. Wildland Fire, 26, 331–344, https://doi.org/10.1071/WF16079, 2017.

Thomas, C. M., Sharples, J. J., and Evans, J. P.: The terminal-velocity assumption in simulations of long-range ember transport, Math. Comput. Simulat., 175, 96–107, https://doi.org/10.1016/j.matcom.2019.08.008, 2020.

Thurston, W., Kepert, J. D., Tory, K. J., and Fawcett, R. J. B.: The contribution of turbulent plume dynamics to

Proof only

long-range spotting, Int. J. Wildland Fire, 26, 317–330, https://doi.org/10.1071/WF16142, 2017.

Trucchia, A., Egorova, V., Butenko, A., Kaur, I., and Pagnini, G.: RandomFront 2.3: a physical parameterisation of fire spotting for operational fire spread models – implementation in WRF-SFIRE and response analysis with LSFire+, Geosci. Model Dev., 12, 69–87, https://doi.org/10.5194/gmd-12-69-2019, 2019.

van der Walt, S., Colbert, S. C., and Varoquaux, G.: The NumPy array: a structure for efficient numerical computation, Comput. Sci. Eng., 13, 22–30, https://doi.org/10.1109/MCSE.2011.37, 2011.

Virtanen, P., Gommers, R., Oliphant, T. E., Haberland, M., Reddy, T., Cournapeau, D., Burovski, E., Peterson, P., Weckesser, W., Bright, J., van der Walt, S. J., Brett, M., Wilson, J., Millman, K. J., Mayorov, N., Nelson, A. R. J., Jones, E., Kern, R., Larson, E., Carey, C. J., Polat, İ., Feng, Y., Moore, E. W., VanderPlas, J., Laxalde, D., Perktold, J., Cimrman, R., Henriksen, I., Quintero, E. A., Harris, C. R., Archibald, A. M., Ribeiro, A. H., Pedregosa, F., and van Mulbregt, P.: SciPy 1.0: fundamental algorithms for scientific computing in Python, Nat. Methods, 17, 261–272, https://doi.org/10.1038/s41592-019-0686-2, 2020.

Werth, P. A., Potter, B. E., Clements, C. B., Finney, M. A., Goodrick, S. L., Alexander, M. E., Cruz, M. G., Forthofer, J. A., and McAllister, S. S.: Synthesis of knowledge of extreme fire behavior: volume I for fire managers, U.S. Department of Agriculture, Forest Service, Pacific Northwest Research Station, Portland, OR, Gen. Tech. Rep. PNW-GTR-854, 144 pp., https://doi.org/10.2737/PNW-GTR-854, 2011.

Werth, P. A., Potter, B. E., Alexander, M. E., Clements, C. B., Cruz, M. G., Finney, M. A., Forthofer, J. M., Goodrick, S. L., Hoffman, C., Jolly, W. M., McAllister, S. S., Ottmar, R. D., and Parsons, R. A.: Synthesis of knowledge of extreme fire behavior: volume 2 for fire behavior specialists, researchers, and meteorologists, U.S. Department of Agriculture, Forest Service, Pacific Northwest Research Station, Portland, OR, Gen. Tech. Rep. PNW-GTR-891, 258 pp., https://doi.org/10.2737/PNW-GTR-891, 2016.

Wickramasinghe, A., Khan, N., and Moinuddin, K.: Determining Firebrand Generation Rate Using Physics-Based Modelling from Experimental Studies through Inverse Analysis, Fire, 5, 6, https://doi.org/10.3390/fire5010006, 2022.

Proof only

Remarks from the typesetter

TS1 Please note that the correction of "inserting text/sentences" is not a small correction such as grammar, technical issues changes. Please note that this change requires approval from the handling editor (as the text was not included in the approved version of the manuscript). Please provide an explanation of why this needs to be changed. We will then ask the editor for approval. Thank you.

TS2 Please see my previous comment in Sect. 2.2.1.